



Influence of quartic anharmonicity on lattice dynamics and thermal transport properties of 16 antiferro structures

Xingzhu Yuan ¹, Yinchang Zhao,^{1,*} Yuming Sun,¹ Jun Ni,^{2,3} and Zhenhong Dai ^{1,†}

¹Department of Physics, *Yantai University*, Yantai 264005, People's Republic of China

²State Key Laboratory of Low-Dimensional Quantum Physics, Department of Physics, *Tsinghua University*, Beijing 100084, People's Republic of China

³Frontier Science Center for Quantum Information, Beijing 100084, People's Republic of China



(Received 12 March 2024; revised 25 May 2024; accepted 25 June 2024; published 8 July 2024)

This paper uses advanced first-principles calculation methods, combined with self-consistent phonon (SCP) theory, compressive sensing (CS) lattice dynamics, and Boltzmann transport equation (BTE), to calculate and study the lattice dynamics and phonon transport of 16 antiferro structures. The lattice thermal conductivity (κ_L) of these materials was studied in detail by analyzing the quartic anharmonic renormalization of phonon frequencies and four-phonon (4ph) scattering, revealing the significant influence of quartic anharmonicity on their thermal transport properties. Our study shows that strong quartic anharmonic renormalization is observed for eight materials, leading to enhanced κ_L . In contrast, for the five materials, the weak quartic anharmonic effect leads to negligible changes in thermal conductivity. Three materials exhibit reduced κ_L due to phonon anharmonic renormalization. Furthermore, 4ph scattering rates (SRs) are important for many of the materials studied and can offset changes in frequency, leading to a reduction in thermal conductivity. At the same time, our calculations give an approximately linear relationship between κ_L and 4ph scattering, which suggests that structures with low κ_L have stronger 4ph scattering. Simultaneously, we chose Li_2O , characterized by high κ_L , and Rb_2Te , known for its low κ_L , to thoroughly examine their microscopic thermal transport mechanisms. This involved detailed analysis of the thermal conductivity spectrum $\kappa_L(\omega)$, scattering phase space, group velocity, and scattering processes. Finally, this study provides insights into the underlying physical mechanisms of thermal transport in 16 antiferro materials and highlights the need to consider 4ph scattering for thermal transport in materials.

DOI: [10.1103/PhysRevB.110.014304](https://doi.org/10.1103/PhysRevB.110.014304)

I. INTRODUCTION

Lattice thermal conductivity (κ_L) is a crucial parameter that quantifies a material's capability to conduct heat, making it a pivotal consideration in material selection for various thermoelectric applications. Recent intriguing advancements, such as predictive first-principles calculations of lattice thermal conductivity [1–3] and the emergence of microscopic experimental probes for accumulating κ_L [4–6], are enriching our comprehension of the physical mechanisms governing thermal transport in solids. The design of future technologies and materials, from waste heat recovery (low κ_L thermoelectric materials) [7,8] to critical needs such as thermal management in nano- and microelectronics (such as high κ_L heat sinks and thermal interface materials) [9,10], depends on a deepening of this understanding. In recent years, there has been an increasing interest in materials with excellent thermoelectric transport properties leading to extensive research on materials with extremely low κ_L values [11–13]. At the same time, the thermal conduction of antiferro (anti- CaF_2 -type) materials has also been widely studied for potential thermoelectric applications [14–16].

The antiferro-type structural materials with fast ionic conductivity have attracted widespread attention due to their technological utility and other remarkable and interesting physical properties. These materials find technical applications in areas such as solid-state batteries, fuel cells, and solid-state gas detectors. Its high ionic conductivity is due to Frankel defects formed by the redistribution of metal atoms at regular sites and interstitial sites. Compared with the FCC oxygen sublattice, the inverse fluorite-type structure has no obvious deformation. This is mainly because the antiferro structure has a looser crystal structure than the fluorite structure. Among the interesting I A-VI A groups, the alkali metal telluride $M_2\text{Se}$ series [$M = \text{Li}, \text{Na}, \text{K}, \text{and Rb}$] [17] has become the focus of numerous theoretical studies, in-depth exploration of some of its basic physical properties. Kikuchi and coworkers [18] performed first-principles density functional calculations of the structural and electronic properties of Li_2Te , Na_2Te , and K_2Te using the full potential linearly enhanced plane wave (FP-LAPW) method. Zhang and coworkers [19] used the PP-PW method to study the lattice dynamics, thermodynamics and elastic properties of Na_2Te . Seifert-Lorenz and Hafner [20] have used the tight-binding linear muffin-tin orbitals (TB-LMTO) approach to study the crystal structure, chemical bonding, and electrical characteristics of several $M_2\text{Te}$ compounds. Experimentally, some

*Contact author: y.zhao@ytu.edu.cn

†Contact author: zhundai@ytu.edu.cn

researchers have also conducted coherent neutron scattering research on Li_2S and Li_2O [21,22]. However, there is a lack of systematic and complete first-principles calculation studies on the thermal transport properties of antiferroite materials. This inspired us to study the microscopic mechanism of lattice thermal transport in 16 antiferroite materials.

For antiferroite materials, despite their relatively simple structures, comprehensive experimental characterization of the thermal transport properties of these compounds and theoretical understanding of the lattice dynamics remains quite challenging. When studying the lattice transport properties of materials, the widely used methods for calculating thermal conductivity are the molecular dynamics (MD) and anharmonic lattice dynamics (ALD) methods. More commonly used are MD-based methods which cover all anharmonic terms and provide a universal expression for κ_L in the Green-Kubo (GK) framework [23,24]. Another approach involves calculating the inharmonic interatomic force constants (IFCs) to solve the classical phonon Peierls-Boltzmann transport equation (BTE) in the simple harmonic approximation (HA) [3,25,26]. However, the calculations obtained on this method are not accurate enough, especially for materials with strong anharmonic interactions. Therefore, it is necessary to consider lattice anharmonicity when calculating phonon eigenvalues [27–29]. Although these two methods are widely used, they are still constrained by computational efficiency and force field accuracy in κ_L modeling of large-scale compounds [30,31]. After decades of development, several calculation methods that consider the lattice anharmonic effect have been proposed for calculating anharmonic phonons at finite temperature [32–36]. These include many-body perturbation theory [37], temperature-dependent effective potential (TDEP) methods [38], and methods combining SCP and compressive sensing (CS) lattice dynamics to determine high-order force constants from force and displacement data training [39–41]. The SCP method can be used for high-throughput calculations because it can quickly handle cubic- and quartic-order anharmonics and calculate anharmonic phonons in large systems [42–44]. Finally, the BTE is solved on the basis of SCP theory, which incorporates the phonon frequency shift caused by four times of anharmonic renormalization. In fact, κ_L is determined by both phonon dispersion and phonon scattering. In addition to considering the change in phonon frequency caused by finite temperature, another important factor is the consideration of phonon scattering caused by lattice anharmonicity. This part comes from the correction of the imaginary part of phonon self-energy by higher-order anharmonicity, which causes changes in three-phonon (3ph) and four-phonon (4ph) scattering, ultimately affecting the relaxation time [45,46]. In summary, it is important to consider quartic-order anharmonicity because it not only results in changes in the phonon scattering rates (SRs) at 3ph and 4ph, but also in temperature-induced anharmonic renormalization of phonon frequencies.

In view of the above problems, this paper uses an advanced first-principles calculation method that combines SCP theory, CS lattice dynamics, and the BTE to calculate the κ_L of a series of antiferroite materials including 3ph and 4ph scattering. By solving the BTE based on the SCP theory, the phonon frequency shift caused by four times of anharmonic renormalization is considered. We calculated parameters such as κ_L

value, scattering process, and phase space for 16 antiferroite materials within a certain temperature range. After analysis, we revealed the underlying mechanism of heat conduction. The results show that comprehensive consideration of the quartic-order anharmonic effect is indispensable for obtaining reasonable κ_L and its variation with temperature. Interestingly, we found that there are some materials with strong quartic-order anharmonicity, and the 4ph scattering rate even exceeds the 3ph scattering rate.

II. METHODOLOGY

Based on the phonon BTE [47], the calculated κ_L tensor is

$$\kappa_L^{\alpha\alpha}(T) = \frac{\hbar^2}{k_B T^2 N_q \Omega} \sum_{\mathbf{q},j} n_{\mathbf{q},j} (n_{\mathbf{q},j} + 1) \omega_{\mathbf{q},j}^2 v_{\mathbf{q},j}^\alpha F_{\mathbf{q},j}^\alpha \quad (1)$$

where \hbar is reduced Planck constant, k_B , T , N_q , and Ω are Boltzmann's constant, absolute temperature, the number of sampled \mathbf{q} wave vectors, and volume of the primitive cell, respectively. The phonon mode-resolved properties, namely, $n_{\mathbf{q},j}$, $\omega_{\mathbf{q},j}$, $v_{\mathbf{q},j}^\alpha$, are the population, frequency, and group velocity along the α axis of the phonon mode, respectively. j and \mathbf{q} specify the phonon mode $|\mathbf{q},j\rangle$. $F_{\mathbf{q},j}^\alpha$ is written as

$$\mathbf{F}_{\mathbf{q},j}^\alpha = \tau_{\mathbf{q},j} (v_{\mathbf{q},j}^\alpha + \Delta_{\mathbf{q},j}), \quad (2)$$

where $\tau_{\mathbf{q},j}$ represents the phonon lifetime under the single-mode relaxation time approximation (SMRTA) [48]. $\Delta_{\mathbf{q},j}$ shows the population deviation of phonons for the SMRTA scheme, used only for the iterative solution of BTE. Normally, except for the $\tau_{\mathbf{q},j}$ parameter in the formula, all other phonon properties can be calculated under HA approximation through the dynamic matrix constructed with simple harmonic IFCs [49,50].

In order to calculate $\tau_{\mathbf{q},j}$ and $\Delta_{\mathbf{q},j}$, a minimum of 3ph scattering process is needed. This may be done by applying perturbation to the HA when dealing with cubic anharmonicity [48], as explained by Eqs. (5)–(9) in Ref. [51]. The above approximation provides a theoretical basis for the calculation of κ_L , and is hereinafter referred to as HA + 3ph and $\kappa_{3\text{ph}}^{\text{HA}}$ for the resultant of κ_L . After only entering quartic anharmonicity, the expressions for $\tau_{\mathbf{q},j}$ and $\Delta_{\mathbf{q},j}$ are Eqs. (2)–(7) in Ref. [52], raising HA + 3ph to HA + 3, 4ph, namely, $\kappa_{3,4\text{ph}}^{\text{HA}}$. In addition, the addition of quartic anharmonicity affects both $\omega_{\mathbf{q},j}$ and $\tau_{\mathbf{q},j}$. $\kappa_{3\text{ph}}^{\text{HA}}$ can be improved when considering the phonon frequency shifts caused by anharmonic phonon renormalization (APRN) at finite temperature. Among the various existing APRN methods [34,36,53,54], we choose the first-order modified SCP theory including quartic anharmonicity to calculate anharmonic phonons [32,55], referred to as SCP + 3ph and $\kappa_{3\text{ph}}^{\text{SCP}}$. It calculates κ_L including only 3ph scattering under SCP theory. In theory, the resulting phonon frequencies are a better representation of the energies of phonon quasiparticles, especially when lattice instability and severe anharmonicity are present [47,56,57]. Finally, the additional phonon scattering rate generated from the 4ph scattering process can be added to the 3ph scattering process [58], forming the most complete theory in the study, namely SCP + 3, 4ph and $\kappa_{3,4\text{ph}}^{\text{SCP}}$.

Density functional theory (DFT), as implemented in the Vienna *Ab initio* Simulation Package (VASP) code, was used for the calculations in this work [59]. Using the projector-enhanced wave potential [60], the generalized gradient approximation (GGA) functional of the Perdure-Burke-Enzerhoff (PBE) [61]. The plane wave cutoff energy is determined to be at least 1.3 times the “ENMAX” value specified in the VASP-recommended projector-augmented wave (PAW) pseudopotential. Given the presence of Li in $\text{Li}_2\text{Se}/\text{Te}/\text{O}/\text{S}$, the cutoff energy for this material is specifically set to 600 eV. For all other materials, the cutoff energy is uniformly set at 500 eV. Cell and atomic degrees of freedom were considered in all structural optimizations, and the convergence criteria for total energy and force were set to 10^{-8} eV and 10^{-4} eV/Å, respectively. The requisite harmonic and anharmonic IFCs are generated within a $2 \times 2 \times 2$ supercell. Specifically, four configurations are generated for the harmonic IFCs in each antiferroite structure using the finite displacement method implemented in the ALAMODE package [47,62]. Therefore, we initiated an *ab initio* molecular dynamics (AIMD) simulation at 300 K, comprising 4000 steps with a 2-fs time step, to acquire 80 snapshot structures. This involved implementing the canonical ensemble with a selected Nosé mass to control the Nosé frequency of temperature oscillations during the simulation, ensuring similarity to the average phonon frequency. Subsequently, the requisite quasirandom configurations employed in first-principles calculations were achieved by introducing 0.1 Å displacements in random directions for each atom within the 80 snapshot structures. In the CS lattice dynamics computations, anharmonic IFCs up to the sixth order are taken into account. This includes interactions up to the fifth (third)-nearest neighbors for cubic (quartic) IFCs, and nearest-neighbor interactions for quintic and sextic IFCs. The precision of anharmonic IFCs relies on the scale of the training dataset, necessitating the sampling of an adequate number of snapshots from the MD trajectories. Because $2 \times 2 \times 2$ supercells are

employed to generate the IFCs, a consistent $2 \times 2 \times 2$ \mathbf{q} mesh is used in the reciprocal-to-real-space Fourier interpolation. Consequently, a highly dense \mathbf{q}_1 mesh of $8 \times 8 \times 8$ is applied to the inner loop of the SCP equation, as illustrated by Eqs. (20)–(23) in Ref. [47]. This approach is crucial for ensuring the convergence of anharmonic phonon eigenvalues. Subsequently, using high-order IFCs as input, the inverse real-space Fourier interpolation method of SCP theory is used to renormalize the inharmonic phonon frequencies. Phonon BTE is solved in $12 \times 12 \times 12$ k-point samples, calculated using a modified version of the shengBTE code FOURPHONON [52,58,63], setting the Gaussian smear to 0.05 eV to simulate the wave vector and associated integral of the phonon. The 3ph process of phonon BTE is solved using an iterative scheme. However, due to the huge computational cost in the iterative solution of the 4ph process, the SMRTA method is used to calculate the 4ph process.

III. RESULTS AND DISCUSSION

Alkali metal chalcogenides A_2B (Li_2O [65,66], Li_2S [67,68], Li_2Se [17,69], Li_2Te [70], Na_2O [65], Na_2S [68,71], Na_2Se [17,71,72], Na_2Te [71,73], K_2O [65,74], K_2S [68], K_2Se [17], K_2Te [75,76], Rb_2O [65,66], Rb_2S [68], Rb_2Se [17], Rb_2Te [76,77]) crystallizes into a cubic antiferroite (anti- CaF_2 type) structure (space group No. 225) [78] at room temperature. Calcium fluoride CaF_2 crystals are one of the most common types of ordered crystals found in nature and are often referred to as fluorite-type structures. The antiferroite structure cubic unit cell contains 12 atoms, among which metal atoms B ($B = \text{O}, \text{S}, \text{Se}, \text{Te}$) occupy the fcc position, located at $(0, 0, 0)$, A ($A = \text{Li}, \text{Na}, \text{K}, \text{Rb}$) atoms occupy Wyck-off positions $(1/4; 1/4; 1/4)$ and $(3/4; 3/4; 3/4)$. Table I lists the calculated lattice constant, dielectric constant, and Born effective charge of these antiferroite materials. The lattice constants of 16 materials calculated using PBE functionals are in good agreement with experimental values. To verify

TABLE I. The calculated lattice constants a^{opt} (in Å), dielectric permittivity tensors (ϵ^∞), Born effective charges (Z^*), temperature dependence of four lattice thermal conductivity coefficients $\kappa_{3\text{ph}}^{\text{HA}}$, $\kappa_{3,4\text{ph}}^{\text{HA}}$, $\kappa_{3\text{ph}}^{\text{SCP}}$ and $\kappa_{3,4\text{ph}}^{\text{SCP}}$ of 16 antiferroite materials. The experimental lattice constant (from Ref. [78]) a^{expt} is listed for comparison.

Material	a^{opt}	a^{expt}	ϵ^∞	$Z^*(A)$	$Z^*(B)$	$\kappa_{3\text{ph}}^{\text{HA}}$	$\kappa_{3,4\text{ph}}^{\text{HA}}$	$\kappa_{3\text{ph}}^{\text{SCP}}$	$\kappa_{3,4\text{ph}}^{\text{SCP}}$
Li_2O	4.620	4.619	3.182	0.993	-1.987	T-1.02	T-1.28	T-0.83	T-1.15
Li_2S	5.700	5.708	3.883	0.950	-1.900	T-0.99	T-1.33	T-0.83	T-1.23
Li_2Se	6.003	6.017	4.346	0.960	-1.920	T-1.08	T-1.42	T-0.86	T-1.30
Li_2Te	6.513	6.517	4.989	0.988	-1.976	T-1.10	T-1.44	T-1.14	T-1.46
Na_2O	5.587	5.560	2.918	0.903	-1.805	T-1.04	T-1.32	T-0.94	T-1.23
Na_2S	6.567	6.550	3.481	0.968	-1.935	T-0.99	T-1.37	T-0.88	T-1.31
Na_2Se	6.850	6.809	3.904	0.982	-1.964	T-0.99	T-1.36	T-0.84	T-1.26
Na_2Te	7.332	7.329	4.307	1.020	-2.040	T-1.00	T-1.35	T-1.01	T-1.45
K_2O	6.481	6.449	3.235	0.905	-1.811	T-1.00	T-1.53	T-0.85	T-1.25
K_2S	7.466	7.391	3.097	0.979	-1.957	T-1.00	T-1.40	T-1.26	T-1.50
K_2Se	7.752	7.676	3.301	0.968	-1.935	T-0.97	T-1.45	T-1.04	T-1.40
K_2Te	8.236	8.168	3.476	0.973	-1.946	T-0.99	T-1.35	T-1.43	T-1.69
Rb_2O	6.871	6.742	3.521	1.038	-2.075	T-0.99	T-1.51	T-1.00	T-1.36
Rb_2S	7.836	7.650	3.180	1.006	-2.013	T-1.01	T-1.45	T-1.07	T-1.38
Rb_2Se	8.122	8.019 [17]	3.333	0.999	-1.979	T-0.99	T-1.35	T-1.22	T-1.56
Rb_2Te	8.607	8.490	3.444	0.988	-1.975	T-0.97	T-1.56	T-1.12	T-1.55

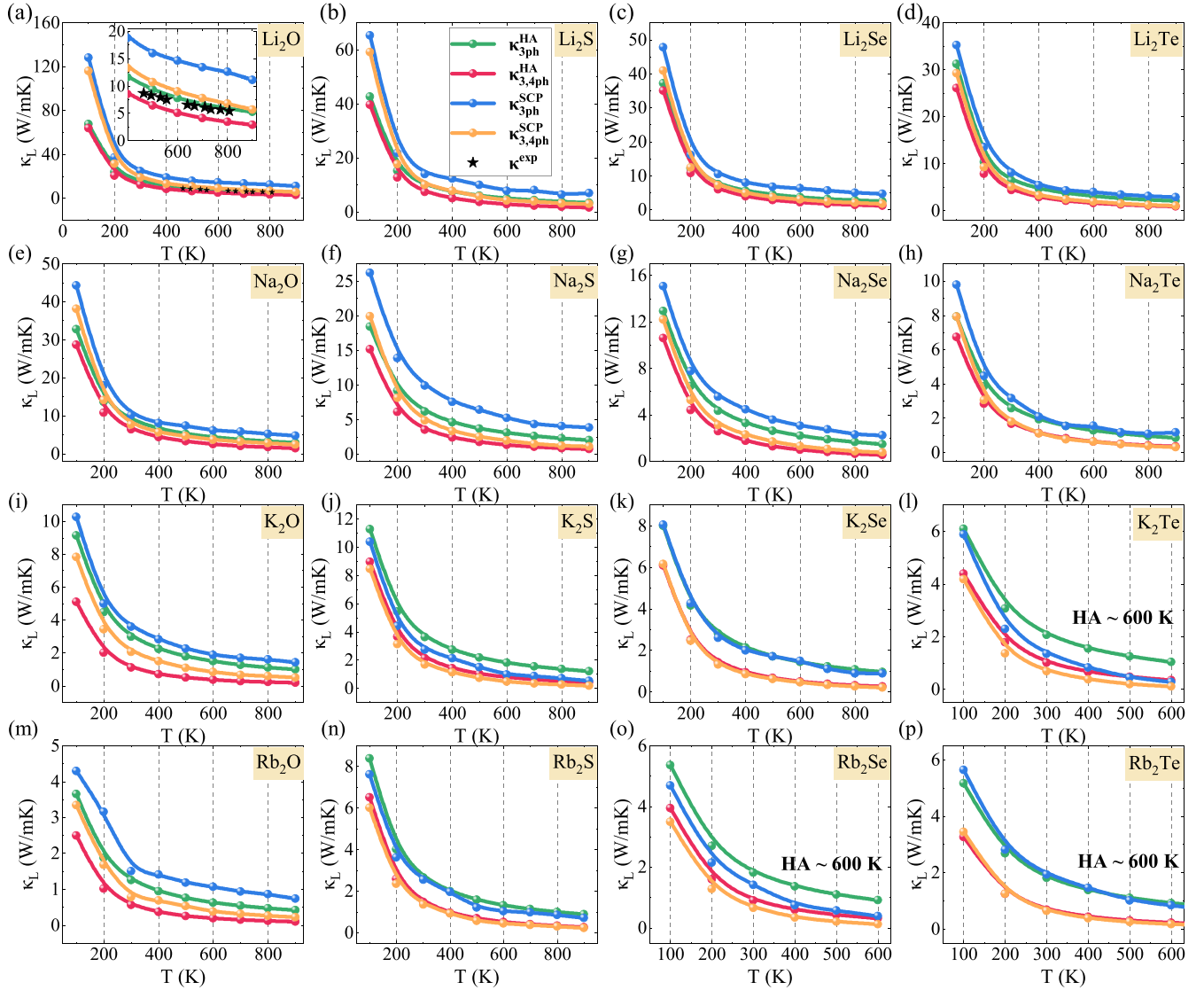


FIG. 1. The relationship between the lattice thermal conductivities $\kappa_{3\text{ph}}^{\text{HA}}$, $\kappa_{3,4\text{ph}}^{\text{HA}}$, $\kappa_{3\text{ph}}^{\text{SCP}}$, and $\kappa_{3,4\text{ph}}^{\text{SCP}}$ and temperature T of four lattice structures of 16 cubic antiperovskite structures: (a) Li_2O , (b) Li_2S , (c) Li_2Se , (d) Li_2Te , (e) Na_2O , (f) Na_2S , (g) Na_2Se , (h) Na_2Te , (i) K_2O , (j) K_2S , (k) K_2Se , (l) K_2Te , (m) Rb_2O , (n) Rb_2S , (o) Rb_2Se , (p) Rb_2Te . The green, pink, blue, and orange lines represent $\kappa_{3\text{ph}}^{\text{HA}}$, $\kappa_{3,4\text{ph}}^{\text{HA}}$, $\kappa_{3\text{ph}}^{\text{SCP}}$, and $\kappa_{3,4\text{ph}}^{\text{SCP}}$ respectively. Experimental values of lattice thermal conductivity κ^{exp} in (a) are represented by black five-pointed stars, which are adapted from Ref. [64]. The inset in (a) is a partially enlarged view of the thermal conductivity of Li_2O lattice.

the plausibility of the calculated dielectric tensor ϵ^∞ and Born effective charge Z^* , we compared the results for Na_2S with experimental values. As shown in Table I, we obtain $\epsilon^\infty = 3.48$, which is basically consistent with the previous experimental value $\epsilon^\infty = 2.96$ [71].

In Fig. 1 we plot the lattice thermal conductivity $\kappa_{3\text{ph}}^{\text{HA}}$, $\kappa_{3,4\text{ph}}^{\text{HA}}$, $\kappa_{3\text{ph}}^{\text{SCP}}$, and $\kappa_{3,4\text{ph}}^{\text{SCP}}$ as a function of temperature T . In this study, we only calculated the contribution of the diagonal terms to the κ_L . In most cases, the contribution of off-diagonal elements is negligible relative to the diagonal terms and can be almost ignored (see Appendix D for specific calculation results). This simplification not only significantly reduces the computational complexity, but also ensures that we accurately analyze the main contribution sources of the κ_L without significantly affecting the accuracy of the results. Since all materials have no imaginary frequencies (phonon spectra under the HA

and SCP approximations are shown in Fig. 10), the $\kappa_{3\text{ph}}^{\text{HA}}$, $\kappa_{3,4\text{ph}}^{\text{HA}}$, $\kappa_{3\text{ph}}^{\text{SCP}}$, and $\kappa_{3,4\text{ph}}^{\text{SCP}}$ provided are all valid. We plotted (a) the experimental κ^{exp} of Li_2O based on data from Ref. [64]. To deeply explore the essence of heat conduction, we use a power law $\kappa_L \propto T^{-\alpha}$ to describe the temperature dependence, as shown in Table I. At extremely low temperatures, κ_L is mainly affected by lattice specific heat and follows the T^3 law. Therefore, we estimate their temperature dependence by considering the effective κ_L values of 16 materials at temperatures $T \geq 200$ K. Starting with $\kappa_{3\text{ph}}^{\text{HA}}$, we can see that the value determined by Li_2O and the experimental value agree well. The calculated $\kappa_{3\text{ph}}^{\text{HA}}$ of Na_2Te , K_2O , K_2Se , K_2Te , and Rb_2S at room temperature are 2.58, 2.98, 2.82, 2.06, and 2.66 $\text{Wm}^{-1}\text{K}^{-1}$ respectively, which is equivalent to the $\kappa_L \sim 2 \text{Wm}^{-1}\text{K}^{-1}$ of the typical thermoelectric material PbTe at room temperature [79,80]. Focusing first on the temperature

dependency, we examine Table I and find that $\alpha \propto 0.97$ to 1.08 in $\kappa_L \propto T^{-\alpha}$ is in line with the present laws of common semiconductors. Under HA, all 16 materials remain stable. After adding $\kappa_{3\text{ph}}^{\text{HA}}$ to 4ph scattering to obtain $\kappa_{3,4\text{ph}}^{\text{HA}}$ through the SMRTA scheme, it was found that $\alpha \propto 1.28$ to 1.56 in $\kappa_L \propto T^{-\alpha}$, the temperature dependence of κ_L was enhanced. Zhao *et al.* [31] also provided evidence of the method's shortcomings. The κ_L solution resulting from the phonon frequency change caused by APRN becomes numerically valid in all selected antifluorite structures, whether only 3ph scattering or 4ph scattering. Furthermore, comparing $\kappa_{3\text{ph}}^{\text{SCP}}$ with $\kappa_{3,4\text{ph}}^{\text{HA}}$, the temperature dependence decreases, with $\alpha \propto 0.83$ to 1.43 in $\kappa_L \propto T^{-\alpha}$. Theoretically, since the quartic anharmonicity is fully included, the most accurate κ_L should be obtained. We only consider the correction of the real part by the quartic anharmonicity because the quartic anharmonicity is a first-order correction and its effect is more significant. The results of the cubic anharmonic correction are detailed in Appendix J. We found that the cubic anharmonic correction is small and can be ignored for the materials studied, but may have an important effect for some materials. In the following discussion, we perform calculations and explanations based on SCP theory. In the Li_2O material, the experimental results are in good agreement with the results of $\kappa_{3\text{ph}}^{\text{HA}}$, and the results of $\kappa_{3,4\text{ph}}^{\text{SCP}}$ are slightly higher than the experimental values. The difference may be due to the fact that we did not consider the grain boundary size in our calculations. The theoretical density of the sample used in the experiment was $70.8 \sim 93.4\%$, and our calculations were based on a perfect crystal lattice without impurities. It is observed in the graph drawn in Fig. 1 that for the eight antifluorite materials $\text{Li}_2\text{O/S/Se}$, $\text{Na}_2\text{O/S/Se}$, K_2O , and Rb_2O , the value of $\kappa_{3\text{ph}}^{\text{SCP}}$ is significantly greater than $\kappa_{3\text{ph}}^{\text{HA}}$. This is because the APRN of these materials causes the phonon spectrum to harden, which raises the phonon frequency and increases the phonon group velocity, as shown by the phonon spectrum in Fig. 10. In addition, the 3ph scattering phase space is often suppressed by phonon spectrum hardening [81,82]. For K_2O and Rb_2O , although the group velocity under the SCP approximation will be reduced compared to the HA approximation, their 4ph scattering is very strong (as shown in Fig. 11). However, for the three materials K_2S , K_2Te , and Rb_2Se , the value of $\kappa_{3\text{ph}}^{\text{HA}}$ is large than $\kappa_{3\text{ph}}^{\text{SCP}}$ because APRN causes the phonon spectrum to soften, the phonon frequency to decrease, and the group velocity to decrease (as shown in Fig. 10). Surprisingly, the results obtained for $\text{Li}_2\text{O/S/Se}$ and Na_2O are very similar. This is caused by two reasons: on the one hand, it is due to the increase in κ_L caused by APRN mentioned above. On the other hand, APRN introduces 4ph scattering when correcting the imaginary part of the self-energy, and the phonon lifetime is reduced, resulting in a decrease in κ_L . These two different results lead to $\kappa_{3\text{ph}}^{\text{HA}}$ and $\kappa_{3,4\text{ph}}^{\text{SCP}}$ being very similar. For the five materials Li_2Te , Na_2Te , Rb_2Te , K_2Se , and Rb_2S , the results obtained for $\kappa_{3\text{ph}}^{\text{HA}}$ and $\kappa_{3,4\text{ph}}^{\text{SCP}}$ are similar, which is consistent with the results of the phonon spectrum in Fig. 10. APRN's real part correction of the phonon self-energy of these four materials is not obvious [81–83]. At the same time, the introduction of 4ph reduces κ_L . In order to compare the calculation results of $\kappa_{3,4\text{ph}}^{\text{SCP}}$ of 16 materials more intuitively, we plot the $\kappa_{3,4\text{ph}}^{\text{SCP}}$ of 16 antifluorite materials at 300 K in order, as shown in

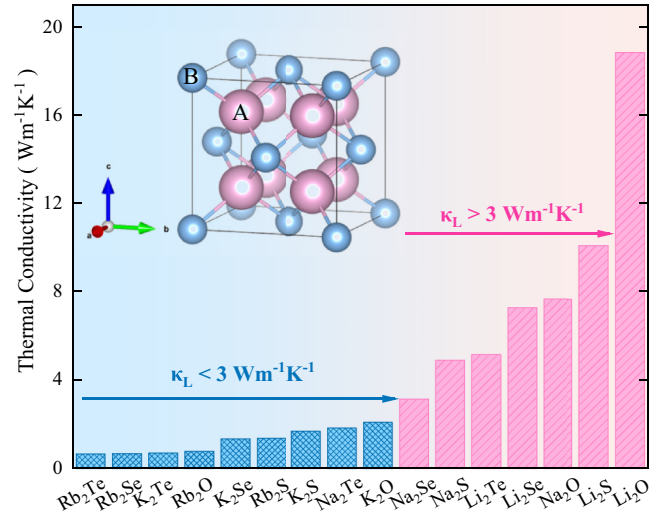


FIG. 2. The 16 antifluorite materials are arranged in ascending order of κ_L at 300 K. The blue area is $\kappa_L < 3 \text{ Wm}^{-1}\text{K}^{-1}$ and the pink area is $\kappa_L > 3 \text{ Wm}^{-1}\text{K}^{-1}$. The illustration is the lattice structure of A_2B ($A = \text{Li, Na, K, Rb}$; $B = \text{O, S, Se, Te}$), where the pink ball represents the A atom, the blue ball represents the B atom.

Fig. 2. We observed that nine materials have values less than $3 \text{ Wm}^{-1}\text{K}^{-1}$ and seven materials have values greater than $3 \text{ Wm}^{-1}\text{K}^{-1}$. At 300 K, the calculated $\kappa_{3,4\text{ph}}^{\text{SCP}}$ of Rb_2Te , Rb_2Se and K_2Te are 0.65, 0.67, and 0.69 $\text{Wm}^{-1}\text{K}^{-1}$ respectively, which is lower compared with traditional half-Heusler materials and thermoelectric materials (as shown in Fig. 17). This finding it provides important ideas for finding materials with low thermal conductivity. The relationship between the 16 antifluorite structures and the average atomic mass \bar{M} is shown in Fig. 3(a). According to the empirical rule given by Slack [84–86], for materials with the same crystal structure, the κ_L decreases as the atomic mass increases. As can be seen from Fig. 3(a), the materials we calculated are in line with past empirical rules. Within the pink region, a decreasing trend with \bar{M} from 18.81 $\text{Wm}^{-1}\text{K}^{-1}$ for light Li_2O to 0.65 $\text{Wm}^{-1}\text{K}^{-1}$ for heavy Rb_2Te is also shown. By considering quartic anharmonic renormalization and the scattering rate of quartic anharmonicity, the calculation of HA + 3ph becomes HA + 3, 4ph, SCP + 3ph, SCP + 3, 4ph. In order to better illustrate the relative change of κ_L , in Fig. 4, we plot the values of $\kappa_{3\text{ph}}^{\text{SCP}}$, $\kappa_{3,4\text{ph}}^{\text{SCP}}$, and $\kappa_{3,4\text{ph}}^{\text{HA}}$ divided by $\kappa_{3\text{ph}}^{\text{HA}}$ and $\kappa_{3,4\text{ph}}^{\text{SCP}}/\kappa_{3\text{ph}}^{\text{SCP}}$ at 300 K. The value of $\kappa_{3,4\text{ph}}^{\text{HA}}/\kappa_{3\text{ph}}^{\text{HA}}$ reflects the influence of additional 4ph scattering on κ_L based on the 3ph process under the HA approximation. The ratio relationship of $\kappa_{3\text{ph}}^{\text{SCP}}/\kappa_{3\text{ph}}^{\text{HA}}$ reflects the importance of the phonon frequency shift due to the finite-temperature effect calculated under the SCP approximation to the calculated antifluorite structure. The value of $\kappa_{3,4\text{ph}}^{\text{SCP}}/\kappa_{3\text{ph}}^{\text{HA}}$ reveals the net effect of full quartic anharmonicity, including quartic anharmonic renormalization of phonon frequencies and 4ph scattering. Firstly, from the ratio of $\kappa_{3,4\text{ph}}^{\text{HA}}/\kappa_{3\text{ph}}^{\text{HA}}$, it can be seen that under the HA approximation, κ_L is significantly reduced after considering 4ph scattering. When APRN is taken into account, for $\text{Li}_2\text{O/S/Se/Te}$, $\text{Na}_2\text{O/S/Se/Te}$, $\text{Rb}_2\text{O/Te}$, and K_2O the $\kappa_{3\text{ph}}^{\text{SCP}}/\kappa_{3\text{ph}}^{\text{HA}}$ ratio exceeds 1, APRN increases the ratio of these materials. Similarly, we can infer

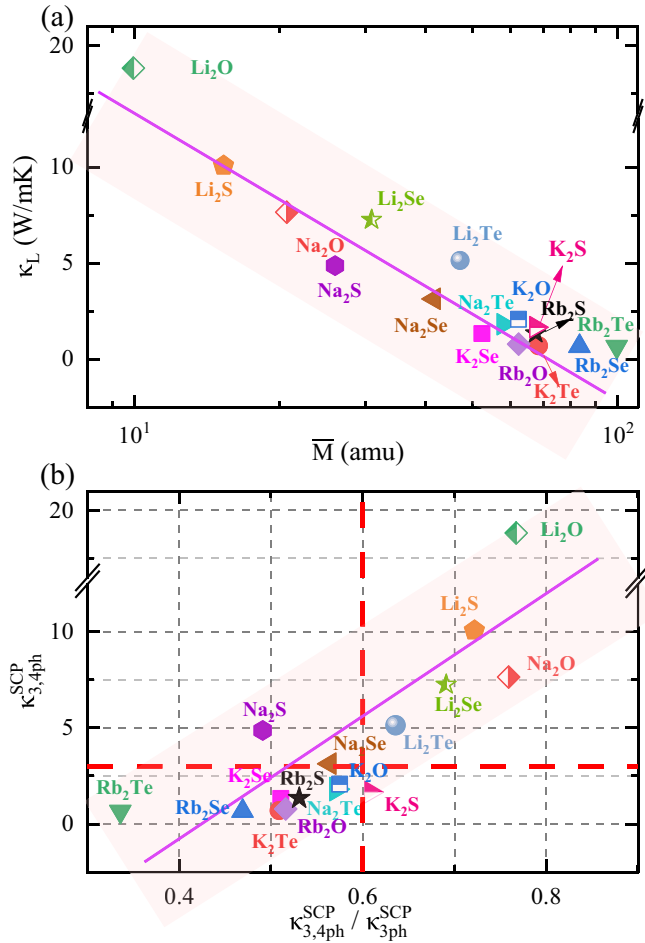


FIG. 3. (a) $\kappa_{3,4ph}^{SCP}$ as a function of average atomic mass, (b) $\kappa_{3,4ph}^{SCP}$ as a function of $\kappa_{3,4ph}^{SCP}/\kappa_{3ph}^{SCP}$ ratio for 16 antifluorites A_2B at 300 K. Except for Li_2O , all data points are located in the pink area.

that Li_2O , Na_2S , and Li_2Se have strong phonon frequency changing effects because their $\kappa_{3ph}^{SCP}/\kappa_{3ph}^{HA}$ ratios are large, exceeding 1.5. Interestingly, $\kappa_{3,4ph}^{HA}/\kappa_{3ph}^{HA}$ and $\kappa_{3,4ph}^{SCP}/\kappa_{3ph}^{SCP}$ have similar information, as they both reflect relative changes due to additional 4ph interactions. However, $\kappa_{3,4ph}^{SCP}/\kappa_{3ph}^{SCP}$ can be used for all structures, but $\kappa_{3,4ph}^{HA}/\kappa_{3ph}^{HA}$ is not suitable for HA phonon frequencies containing imaginary frequencies. It can be observed in Fig. 4 that the $\kappa_{3,4ph}^{SCP}/\kappa_{3ph}^{SCP}$ values of Li_2Te , $\text{Na}_2\text{S}/\text{Se}/\text{Te}$, $\text{K}_2\text{O}/\text{S}/\text{Se}/\text{Te}$, and $\text{Rb}_2\text{O}/\text{S}/\text{Se}$ are between 0.47 and 0.64, indicating that the 4ph SRs and 3ph SRs are comparable. In addition, the phonon frequency shift caused by 4ph scattering and finite temperature effects compete for the final effect. Specifically, the value of $\kappa_{3,4ph}^{SCP}/\kappa_{3ph}^{HA}$ of $\text{Li}_2\text{S}/\text{Se}$ is ~ 1 , indicating that the quartic anharmonic renormalization of the phonon frequency is equivalent to the 4ph scattering effect. $\text{Li}_2\text{O}/\text{S}/\text{Se}$ exhibits values of $\kappa_{3,4ph}^{SCP}/\kappa_{3ph}^{HA} > 1$, meaning that for the contribution, the phonon frequency shift is greater than 4ph scattering. For other materials with a $\kappa_{3,4ph}^{SCP}/\kappa_{3ph}^{HA}$ value < 1 , the opposite is true. Overall, it is crucial to consider the net effect of full quartic anharmonicity.

From the ratio of $\kappa_{3,4ph}^{SCP}/\kappa_{3ph}^{SCP}$ we can find that some antifluorite structures have strong 4ph scattering. In order to observe the relationship between 4ph and the obtained, the ratio of $\kappa_{3,4ph}^{SCP}$ to $\kappa_{3,4ph}^{SCP}/\kappa_{3ph}^{SCP}$ at 300 K is plotted in Fig. 3(b). Overall,

we found a roughly linear relationship between $\kappa_{3,4ph}^{SCP}$ and $\kappa_{3,4ph}^{SCP}/\kappa_{3ph}^{SCP}$ for the 16 antifluorite materials, suggesting that smaller materials have lower $\kappa_{3,4ph}^{SCP}/\kappa_{3ph}^{SCP}$ ratios and therefore stronger 4ph scattering. This is shown in the data points in the pink area in Fig. 3(b). Especially for Rb_2Te and Rb_2Se , it is $\kappa_L < 1 \text{ Wm}^{-1}\text{K}^{-1}$ at 300 K, and its 4ph and 3ph scattering are equivalent, which can be proved by the result of $\kappa_{3,4ph}^{SCP}/\kappa_{3ph}^{SCP} < 0.5$.

We examine in detail the role of quartic anharmonicity in the two cases of high κ_L and low κ_L that we have chosen below: Li_2O and Rb_2Te . Rb_2Te is special because the anti- CaF_2 structure it forms at room temperature is metastable, but if the temperature is too high, it will irreversibly transform into the PbCl_2 -resistant structure [70] type, so we only consider 600 K. In Figs. 5(a) and 5(d), we plot the phonon dispersion curves and density of states (DOS) calculated under the HA and SCP approximations for the two materials. The renormalized phonon frequency may be significantly affected by the underlying strong 4ph anharmonic frequency. As shown in Figs. 5(a) and 5(d), the phonon spectrum curves of the two materials show obvious temperature-dependent behavior. It can be observed that there is no imaginary frequency in both materials, indicating that they are dynamically stable. In addition, it was found that the phonon spectrum of the two materials has an obvious depression at point L, where Rb_2Te undergoes significant hardening. Especially in low-frequency acoustic modes, SCP theory often causes a hardening of the phonon spectrum, usually due to the positive and dominant contribution of the diagonal term of the quartic anharmonicity to the phonon eigenvalues. Harmonic effects usually increase the frequency of lower-order modes. After phonon renormalization, we observed that temperature has a significant impact on the renormalized phonon energy, and Li_2O is significantly hardened mainly in the range 250–to 420 cm^{-1} . These phonon modes are mainly contributed by the vibration of Li atoms and O atoms, as shown in the anharmonic phonon density of states (AHPDOS) at 300 K in Fig. 5. In contrast, the high-frequency optical modes corresponding to the majority Li atomic contributions are only slightly hardened. For Rb_2Te , as the temperature increases, the low-frequency phonon branches harden, while the intermediate-frequency and high-frequency optical modes soften significantly. But acoustic phonons dominate, accounting for about 86%. In addition, it can be seen from the insets of Figs. 5(c) and 5(f) that the high-energy mode of Li_2O above approximately $\omega > 420 \text{ cm}^{-1}$ is mainly determined by the vibration of Li atoms, which have the largest MSDs due to their lighter mass. For Rb_2Te , the high-frequency mode above about $\omega > 60 \text{ cm}^{-1}$ is mainly contributed by the lighter mass Rb atoms, and its maximum MSDs leads to the softening of the high-frequency optical phonon mode. Although the MSDs of O atoms and Te atoms is smaller, their vibrations are also broadened.

In order to better understand their lattice dynamics and thermal transport properties, elucidate the origin and the role of 4ph scattering, we analyzed the 4ph theory of κ_{3ph}^{SCP} and $\kappa_{3,4ph}^{SCP}$ at room temperature and the cumulative values of Li_2O and Rb_2Te , as shown in Figs. 5(b) and 5(e). The majority of lattice heat conduction is carried by low-frequency phonons, such as those with frequency $\omega < 420$ (60) cm^{-1} in Li_2O

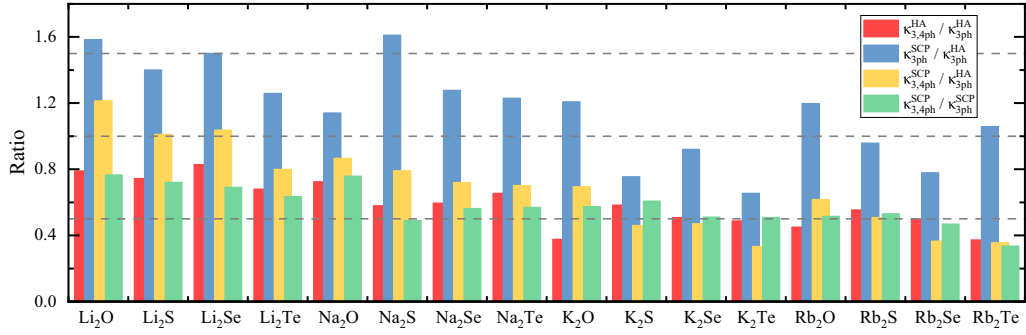


FIG. 4. Calculated $\kappa_{3,4ph}^{HA}/\kappa_{3ph}^{HA}$, $\kappa_{3ph}^{SCP}/\kappa_{3ph}^{HA}$, $\kappa_{3,4ph}^{SCP}/\kappa_{3ph}^{HA}$, and $\kappa_{3,4ph}^{SCP}/\kappa_{3,4ph}^{SCP}$ ratio relationship of 16 antiperovskite materials A_2B at 300 K.

(Rb_2Te), as can be seen from the image. Simultaneously, due to the presence of 4ph scattering, the thermal conductivity spectrum $\kappa_{3,4ph}^{SCP}(\omega)$ is significantly reduced relative to $\kappa_{3ph}^{SCP}(\omega)$, especially in Rb_2Te . Therefore, the cumulative κ_L value of the SCP + 3ph model exceeds the cumulative value of the SCP + 3, 4ph model, and the final $\kappa_{3,4ph}^{SCP}$ of Li_2O (Rb_2Te) is only about 76% (34%) of κ_{3ph}^{SCP} . At room temperature, the calculated κ_{3ph}^{SCP} and $\kappa_{3,4ph}^{SCP}$ values of Li_2O (Rb_2Te) are 24.54 (1.93) and 18.81 (0.65) $Wm^{-1}K^{-1}$, respectively. After considering 4ph scattering, Li_2O (Rb_2Te) significantly reduced at room temperature, reaching 23.35% (66.32%), as shown in Fig. 6. In order to observe the bonding situation of the two materials in more detail, in Figs. 5(c) and 5(f), we plot the integrated crystal orbital Hamiltonian population (ICOHP)

diagram. For both materials, the $-ICOHP$ of the Li-O bond and the Rb-Te bond is larger and forms an ionic bond.

Next, we explore the mechanism of lattice conduction, and the 3ph and 4ph scattering processes at 300 K are compared in Figs. 7(a) and 7(b). We can see that 4ph scattering in Rb_2Te is comparable to 3ph scattering in the frequency range 40–60 cm^{-1} , while in Li_2O 4ph scattering is significantly lower than 3ph. For K_2O , K_2Te , Rb_2Se , Rb_2S , Na_2Se , and Na_2S , 4ph scattering is equivalent to 3ph scattering within a certain frequency, as can be seen in Fig. 11. In addition, as the temperature increases, the 4ph scattering of Rb_2Te at 600 K is significantly stronger than that of 3ph, as shown in Fig. 12, where the 4ph process of Li_2O is also comparable to the 3ph process at high temperature of 900 K. In order to test the applicability of the phonon quasiparticle image, the

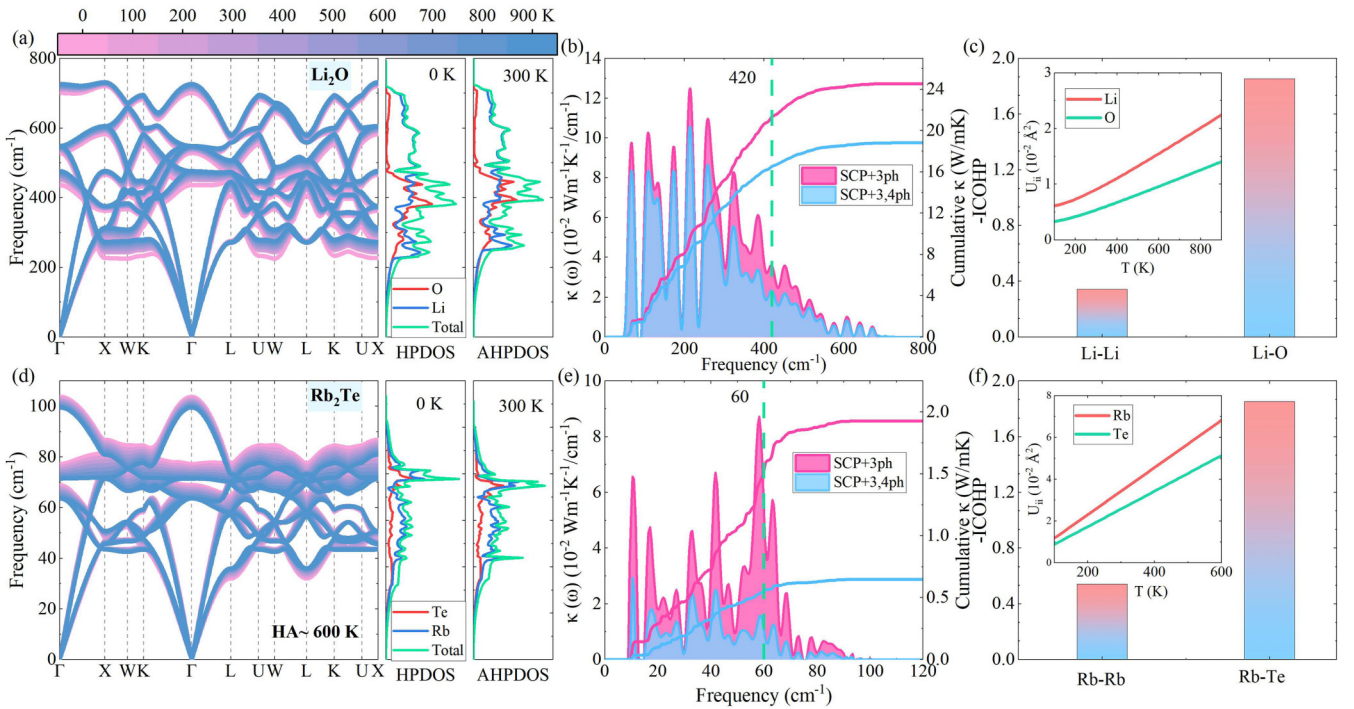


FIG. 5. (a) Calculated temperature-dependent phonon spectrum and density of states diagram for Li_2O . HA is 0 K, 100 to 900 K are the results of SCP approximate calculations. (b) Thermal conductivity spectrum $\kappa_L(\omega)$ and cumulative κ_L of Li_2O at 300 K as a function of frequency. The pink and blue areas and solid lines represent calculations under the SCP + 3ph and SCP + 3,4ph models, respectively. (c) Values of $-ICOHP$ for Li-Li and Li-O bonds in Li_2O . The inset shows the mean-square displacements (MSDs) of atoms as a function of temperature from 100 to 900 K. (d)–(f) are the same as (a)–(c), but for Rb_2Se .

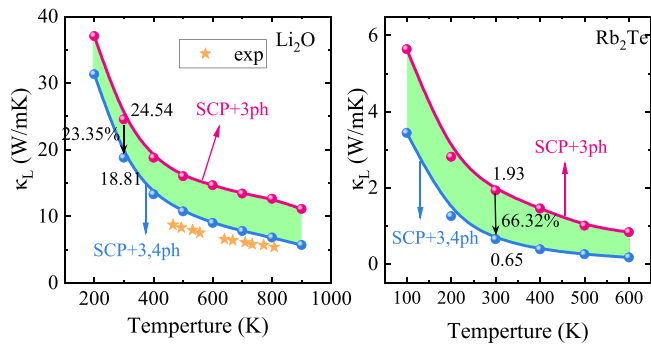


FIG. 6. Values of κ_L calculated in the SCP + 3ph and SCP + 3, 4ph models, Li_2O from 100 to 900 K, and Rb_2Te from 100 to 600 K. The pink and blue lines represent calculations under the SCP + 3ph and SCP + 3, 4ph models, respectively. The green area represents the difference between $\kappa_{3\text{ph}}^{\text{SCP}}$ and $\kappa_{3,4\text{ph}}^{\text{SCP}}$, and the orange five-pointed star is the experimental value κ_L^{exp} .

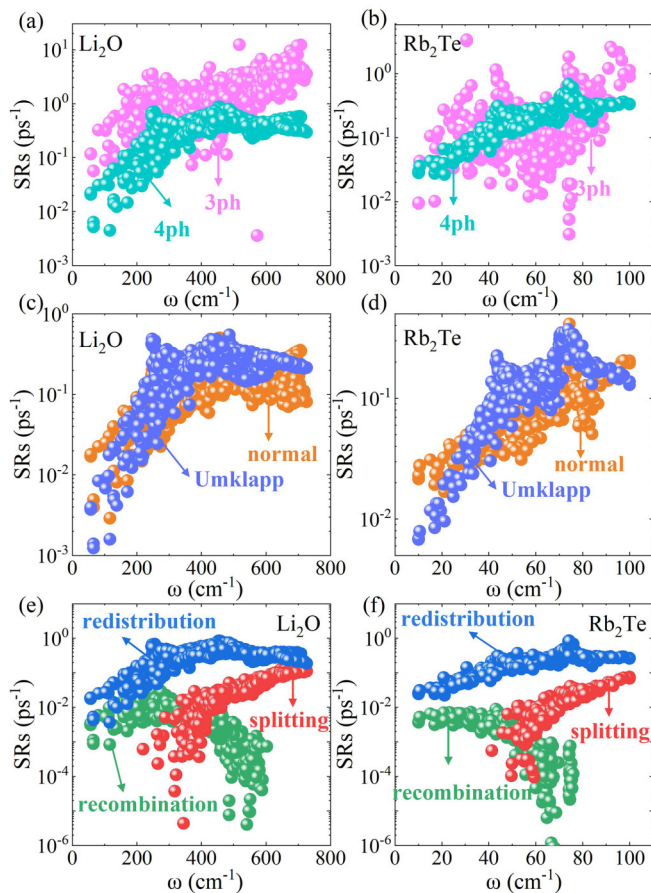


FIG. 7. Scattering rates of Li_2O and Rb_2Te (a) Cubic Li_2O at 300 K for 3ph and 4ph SRs, which are represented by light magenta and cyan blue spheres respectively. (c) The 4ph scattering of Li_2O is divided into normal process and Umklapp process, which are represented by orange and purple spheres respectively. (e) Decompose the 4ph scattering rate into splitting ($\lambda \rightarrow \lambda_1 + \lambda_2 + \lambda_3$), redistribution ($\lambda + \lambda_1 \rightarrow \lambda_2 + \lambda_3$) and recombination ($\lambda + \lambda_1 + \lambda_2 \rightarrow \lambda_3$), which are represented by red, green and blue spheres respectively express. (b), (d), and (f) are the same as (a), (c), and (e) respectively, but for Rb_2Te .

curve of SRs equal to the phonon frequency is also drawn in Figs. 11 and 12, that is, $1/\tau = \omega/2\pi$, that is, the phonon lifetime τ is equivalent to the vibration period of the phonon quasiparticle. Once SRs exceed the curve of $1/\tau = \omega/2\pi$, the phonon lifetime τ is less than one vibration period (the phonon annihilates before completing one vibration), so the phonon quasiparticle image is no longer valid. As shown in Figs. 11 and 12, most of the 3ph and 4ph scatterings are distributed below the $1/\tau = \omega/2\pi$ curve, supporting the validity of the BTE solution in this article. However, in Fig. 11, the 3ph SRs of Rb_2O mostly exceed the quasiparticle image. Since the anharmonic 3ph and 4ph scattering are both very strong, other methods are needed for calculation. In order to further explore the potential mechanism of 4ph scattering, the 3ph and 4ph scattering phase spaces (P_3 and P_4) of Li_2O and Rb_2Te at 300 K were also analyzed, as shown in Figs. 9(b) and 9(d). We found that the 4ph scattering phase space (P_4) of the two materials is almost the same as the 3ph scattering phase space (P_3), and even P_4 exceeds P_3 in a certain area. It can also be seen from the illustration that P_4/P_3 are both greater than 1. Figures 9(a) and 9(c) show the phonon dispersion of Li_2O and Rb_2Te respectively, and the mode-dependent Grüneisen parameters are also projected onto each phonon band. The color map from brown to green represents the interval from 0 to 3 for the Grüneisen parameter. It can be seen from the figure that the larger γ of Li_2O is densely distributed in the range 200–400 cm^{-1} , while the larger γ of Rb_2O is distributed in the range 40–60 cm^{-1} and 70–90 cm^{-1} . Generally speaking, compared with the high-frequency optical mode, the γ of the acoustic mode is larger, indicating that the cubic anharmonicity of the acoustic mode is larger. Furthermore, their phonon modes all show γ close to zero near the γ point. When the optical branch becomes softer, optical acoustic (OA) phonon hybridization needs to be considered. The softening of optical phonons can be thought of as providing more scattering channels.

Next, in order to explore more details of 4ph scattering, as shown in Figs. 7(e) and 7(f), we decompose 4ph scattering into three separate parts, namely the splitting process ($\lambda \rightarrow \lambda_1 + \lambda_2 + \lambda_3$), the redistribution process ($\lambda + \lambda_1 \rightarrow \lambda_2 + \lambda_3$) and recombination process ($\lambda + \lambda_1 + \lambda_2 \rightarrow \lambda_3$), where a is the abbreviation of mode $|\mathbf{q}j\rangle$. From the figure, we find that the redistribution process of Li_2O and Rb_2Te is better than the splitting and recombination process, which can be explained from the perspective of their associated scattering phase space. Considering the limitation of phonon energy conservation during the scattering process, it is estimated that the splitting process is related to the high-frequency phonon mode, while the recombination process is mainly related to the low-frequency phonon mode [93]. The redistribution process is more flexible in satisfying energy conservation. Through analysis, it is found that it will contribute to more 4ph scattering events, thereby playing a dominant role in the scattering phase space and scattering rate. Therefore, the recombination process dominates both the 4ph scattering rate and the scattering phase space, as shown in Figs. 7, 9(c), and 9(f). In addition, 4ph scattering can also be divided into normal and Umklapp processes. As shown in Figs. 7(c) and 7(d), the Umklapp process exceeds the normal process in both Li_2O and Rb_2Te . A similar situation in which the

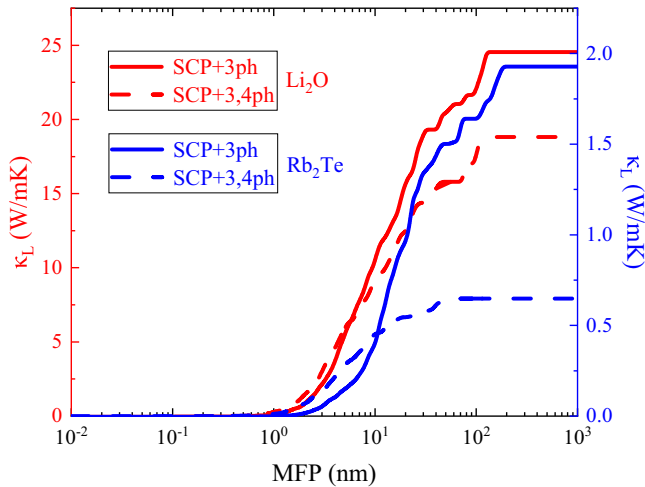


FIG. 8. The MFP cumulative κ_L with and without 4ph scattering for Li_2O and Rb_2Te . The red and blue lines represent the results for cubic Li_2O and Rb_2Te , scaled by the left and right edges, respectively. The solid lines represent results within the SCP + 3ph model, and the dotted lines represent values within SCP + 3, 4ph.

Umklapp process dominates can also be found in the 16 antifluorite structures, as shown in Fig. 13, which demonstrates the rationality of using the SMRTA scheme in the BTE solution to handle the 4ph scattering process for all 16 materials.

In addition, the commonly used physical quantities that reveal different κ_L sources include phonon frequency $\omega_{\mathbf{q},j}$ and group velocity $v_{\mathbf{q},j}$. From the results from HA to SCP, $\omega_{\mathbf{q},j}$ and $v_{\mathbf{q},j}$ are generally enhanced by quartic anharmonic renormalization in the low frequency range of κ_L . Furthermore, according to SCP calculations, this enhancement becomes more obvious at high temperatures, as shown in Fig. 14 for $v_{\mathbf{q},j}$ in Li_2O and Rb_2Te . The difference is that the low-frequency $v_{\mathbf{q},j}$ at 300 K in the SCP in Rb_2Te is 77% lower than that in Li_2O . In addition, the 3, 4ph scattering of Rb_2Te and Li_2O is similar, making the final κ_L in Li_2O about one order of magnitude higher than that in Rb_2Te .

Next, we explore the cumulative κ_L as a function of the maximum mean-free path (MFP) in the SCP + 3ph and SCP + 3, 4ph models to illustrate the impact of the 4ph scattering process on the size dependence of thermal conduction. The MFP accumulation κ_L of Li_2O and Rb_2Te at 300 K is plotted in Fig. 8. For the approximate range of SCP + 3ph and SCP + 3, 4ph, the total cumulative κ_L increases with the increase of MFP until it finally reaches a stable level. For Li_2O , MFP is equal to 126 (114) nm under the SCP + 3ph (SCP + 3, 4ph) approximation; for Rb_2Te , MFP is equal to 182 (49) nm. Obviously, at SCP + 3, 4ph, the maximum MFP of Li_2O is much larger than that of Rb_2Te , which is consistent with the higher phonon $v_{\mathbf{q},j}$ in Li_2O , as shown in Fig. 15. Compared with the results under the SCP + 3ph approximation, the cumulative κ_L of MFP calculated under SCP + 3, 4ph, 4ph reduces the maximum MFP in Li_2O (Rb_2Te) from 126 (182) nm to 114 (49) nm. In addition, when the MFP length in Li_2O (Rb_2Te) exceeds 11 (6) nm, 4ph scattering strongly inhibits the heat transfer of hot carriers. More interestingly,

the heat transfer performance of hot carriers with MFP below 6 nm in Rb_2Te is significantly enhanced by 4ph scattering, as shown in Fig. 8. In addition, through nanostructures, it can be reduced, for example, to $9.44 \text{ Wm}^{-1}\text{K}^{-1}$ when the nanometer size of Li_2O is less than 10 nm.

Finally, our calculations show that even higher-order anharmonicities are important, as shown by the fact that the quartic anharmonicity exceeds the three-phonon image, especially at high temperatures and when the anharmonicity is large. At the same time, we note that the phonon frequency shift caused by cubic anharmonicity and quartic effects is not considered in the current SCP calculations. If these effects are taken into account, the hardening of low-frequency phonons may be slightly limited, resulting in a possible slight reduction in the calculated κ_L . However, the SMRTA protocol used to handle 4ph scattering in the BTE solution provides a slightly underestimated κ_L . Although the fact that the Umklapp process is better than the normal process shows the rationality of the SMRTA scheme, this offsets the impact on the final κ_L to a certain extent, that is, the impact caused by neglecting quasiharmonic effects and phonon frequency shifts. As an outlook, the improved SCP theory can consider both quartic and cubic anharmonicity, that is, the first-order to second-order energy correction of the phonon eigenvalues is included in the calculation of anharmonic phonons. A fully iterative approach proposes to consider both 3ph scattering and 4ph processes in future calculations of κ_L , although this may require significant computational resources.

IV. CONCLUSIONS

In summary, in this paper we systematically studied the effects of quartic anharmonicity on the lattice dynamics and thermal transport properties of 16 antifluorite structures (Li_2O , Li_2S , Li_2Se , Li_2Te , Na_2S , Na_2Se , Na_2Te , K_2O , K_2S , K_2Se , K_2Te , Rb_2O , Rb_2S , Rb_2Se , Rb_2Te). This is achieved through advanced high-throughput first principles, combined with Cs technology, SCP theory and phonon BTE. In addition, by combining the influence of the quartic anharmonic renormalization of phonon frequencies and 4ph scattering, a detailed study and analysis of the lattice thermal conductivities $\kappa_{3\text{ph}}^{\text{HA}}$, $\kappa_{3,4\text{ph}}^{\text{HA}}$, $\kappa_{3\text{ph}}^{\text{SCP}}$, $\kappa_{3,4\text{ph}}^{\text{SCP}}$ of 16 materials was conducted, revealing the quartic anharmonic. The properties have a significant impact on the lattice thermal conductivity of 16 antifluorite structures.

Specifically, strong quartic anharmonic renormalization of phonon frequencies caused by quartic anharmonicity was observed in eight materials ($\text{Li}_2\text{O/S/Se}$, $\text{Na}_2\text{O/S/Se}$, K_2O , Rb_2O), which improved the lattice thermal conductivity. Among the other five antifluorite materials (Li_2Te , Na_2Te , Rb_2Te , K_2Se , Rb_2S), the quartic anharmonic renormalization is weak, making the change in lattice thermal conductivity negligible. For the other three materials (K_2S , K_2Te , Rb_2Se), the phonon anharmonic renormalization reduces the lattice thermal conductivity. In addition, the 4ph SRs is important for many of the materials studied and can offset frequency changes, resulting in a decrease in thermal conductivity. When the 4ph SRs and phonon frequency shift are fully considered, the calculated lattice thermal conductivity is close to the experimental value. By correlating lattice thermal conductiv-

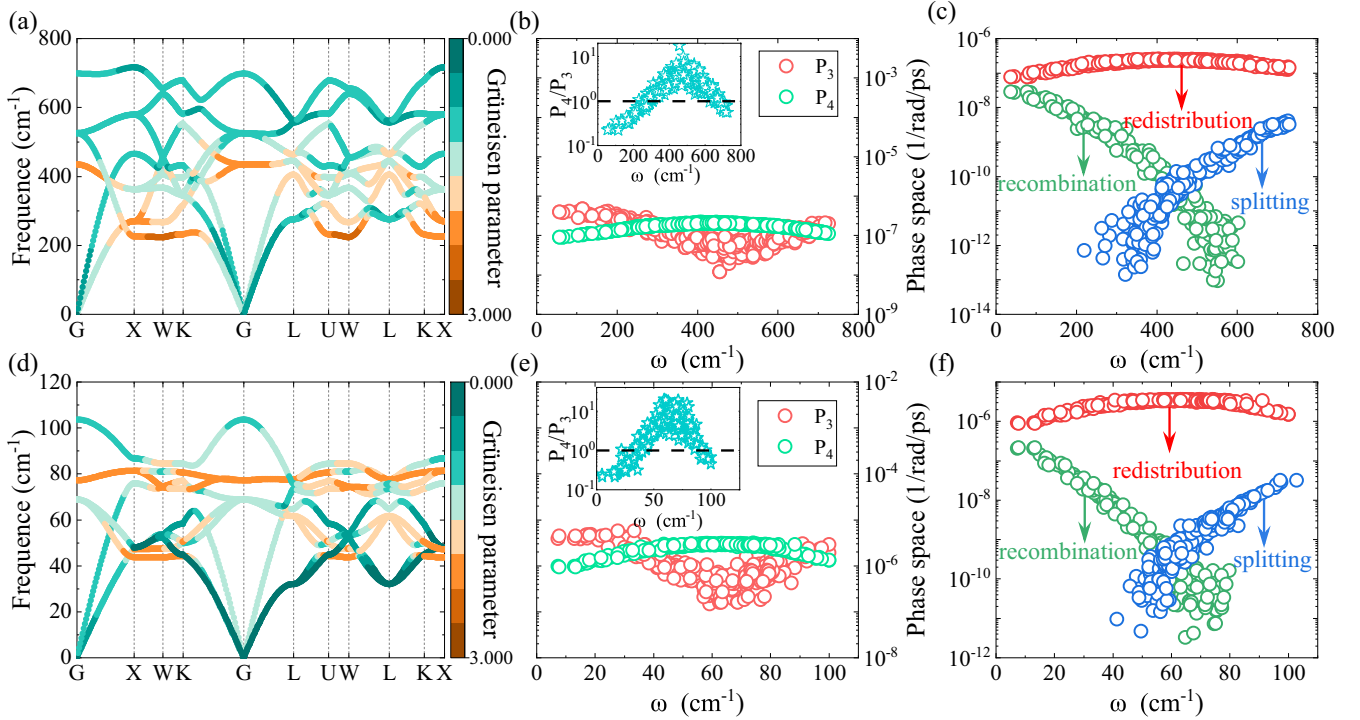


FIG. 9. (a) Calculated phonon spectrum of Li_2O under the HA approximation. The color projection is the Grüneisen parameter. The color bar on the right represents from 0 to 3. (b) Comparison of 3ph and 4ph scattering phase spaces based on SCP theory for Li_2O . The inset shows the frequency resolution ratio of the scattering phase space P_4 - P_3 . (c) Decomposition of P_4 into three processes, namely splitting ($\lambda \rightarrow \lambda_1 + \lambda_2 + \lambda_3$), redistribution ($\lambda + \lambda_1 \rightarrow \lambda_2 + \lambda_3$), and recombination ($\lambda + \lambda_1 + \lambda_2 \rightarrow \lambda_3$), for Li_2O . (d)–(f) are the same as (a)–(c), but for cubic Rb_2Te .

ity and phonon scattering phase space, we demonstrate that the importance of 4ph scattering relative to 3ph scattering can be evaluated qualitatively from the ratio of 4ph to 3ph scattering phase space. At the same time, our calculations give a roughly linear relationship between κ_L and 4ph scattering, which indicates that structures with low κ_L have strong 4ph scattering. In addition, through the analysis of thermal conductivity spectrum $\kappa_L(\omega)$, scattering phase space, group velocity and scattering process, the reason why Li_2O has the highest κ_L and Rb_2Te has the lowest κ_L is explained. The 4ph SRs of Rb_2Te exhibit comparable performance to 3ph SRs in the low-frequency phonon mode, resulting in significant suppression of thermal transport properties. When 4ph scattering is taken into account, the thermal conductivity of Rb_2Te decreases significantly, decreasing by 66.32% at room temperature. In addition, the group velocity of Rb_2Te is 77% lower than that of Li_2O . Ultimately, the κ_L of Rb_2Te is much lower than that of Li_2O at room temperature. In addition, the redistribution process and Umklapp process dominate the strong 4ph scattering, which also shortens the maximum MFP, thereby changing the heat transfer performance of certain MFP-specific hot carriers.

Finally, this study highlights the underlying physical mechanisms of heat transport in 16 antiferroite materials and provides useful insights into the necessity of considering the impact of the 4ph effect on material heat transport.

ACKNOWLEDGMENTS

This research were supported by the Natural Science Foundation of Shandong Province under Grant No. ZR2023ZD09 and by the National Natural Science Foundation of China under Grants No. 12174327, No. 11974302, and No. 92270104.

APPENDIX A: PARTIAL STRUCTURAL INFORMATION OF 16 ANTIFLUORITE STRUCTURES

The dynamic and mechanical properties of crystals are closely related to their elastic constants. These elastic constants play a key role in shaping material strength, defining the material's properties during stress application, deformation and recovery. A cubic crystal has three independent single crystal elastic constants, namely C_{11} , C_{12} , and C_{44} . Among them, C_{11} is closely related to unidirectional compression in the main crystal direction, while C_{44} reflects the resistance against shear deformation. The elastic constants we calculated for 16 materials are listed in Table II together with the existing experimental data and other calculation results. The requirements for mechanical stability of cubic structures are

$$C_{11} - C_{12} > 0, \quad C_{11} + 2C_{12} > 0, \quad C_{44} > 0. \quad (\text{A1})$$

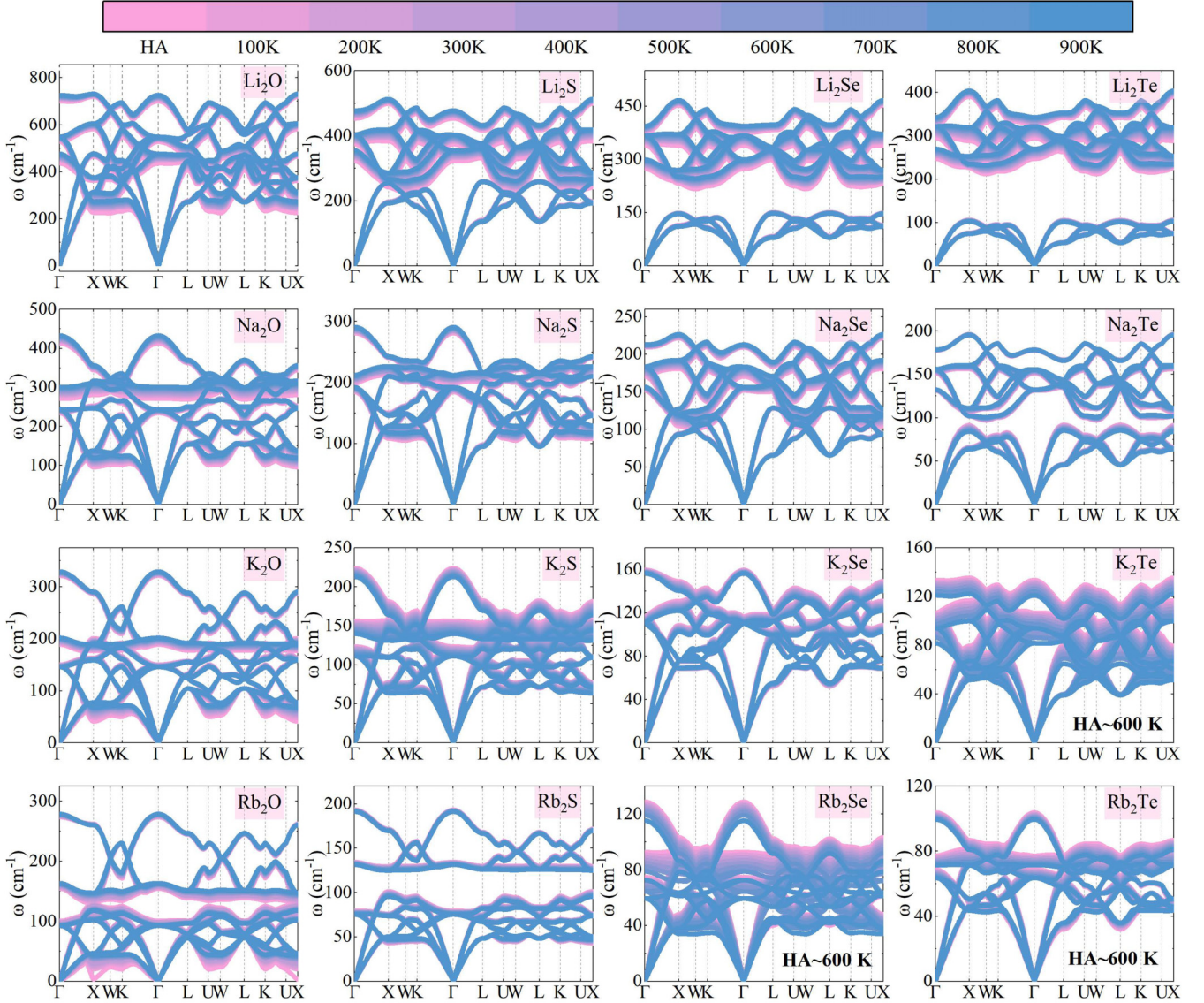


FIG. 10. The calculated temperature-dependent phonon dispersion curves of 16 antifluorite materials are Li_2O , Li_2S , Li_2Se , Li_2Te , Na_2S , Na_2Se , Na_2Te , K_2O , K_2S , K_2Se , K_2Te , Rb_2O , Rb_2S , Rb_2Se , Rb_2Te . HA is 0 K. Except for K_2Te , Rb_2Se , and Rb_2Te are considered at 600 K, other materials are considered at 900 K.

The elastic constants calculated in Table II satisfy the above stability criteria, indicating that these compounds are elastically stable.

Furthermore, in order to study the stiffness of A_2B , several parameters including bulk modulus (B), shear modulus (G), Young's modulus (Y), and Poisson's ratio (ν) were determined using the calculated elastic constants C_{11} , C_{12} , C_{44} . Poisson's ratio is a good characterization of bonding properties in materials. It can formally take values between 0.0 and 0.5.

APPENDIX B: PHONON DISPERSION CURVES OF HA AND SCP FOR 16 ANTIFLUORITE MATERIALS AT DIFFERENT TEMPERATURES

The phonon dispersion curves of 16 antifluorite materials under the HA and SCP approximations are shown in Fig. 10.

There is no imaginary frequency under the HA approximation for 16 materials, which not only illustrates the dynamic stability of these structures, but also means the validity of the data of the BTE solution within the HA. When the quartic anharmonic renormalization of phonon frequencies is considered, the phonon spectrum curves of most materials show obvious temperature-dependent behavior. For most materials, hardening occurs after quartic anharmonic renormalization, resulting in an increase in lattice thermal conductivity. At the same time, in order to illustrate the rationality of our calculations, the comparison of the phonon dispersions of Li_2O [96] and Li_2S [21] with their corresponding experimental values of measured dispersion is plotted in Fig. 16. We found that the calculated results in the low-frequency acoustic mode are in good agreement with the experimental values, and there is a deviation in the highest frequency optical branch. However, since the contribution of the high-frequency optical mode to

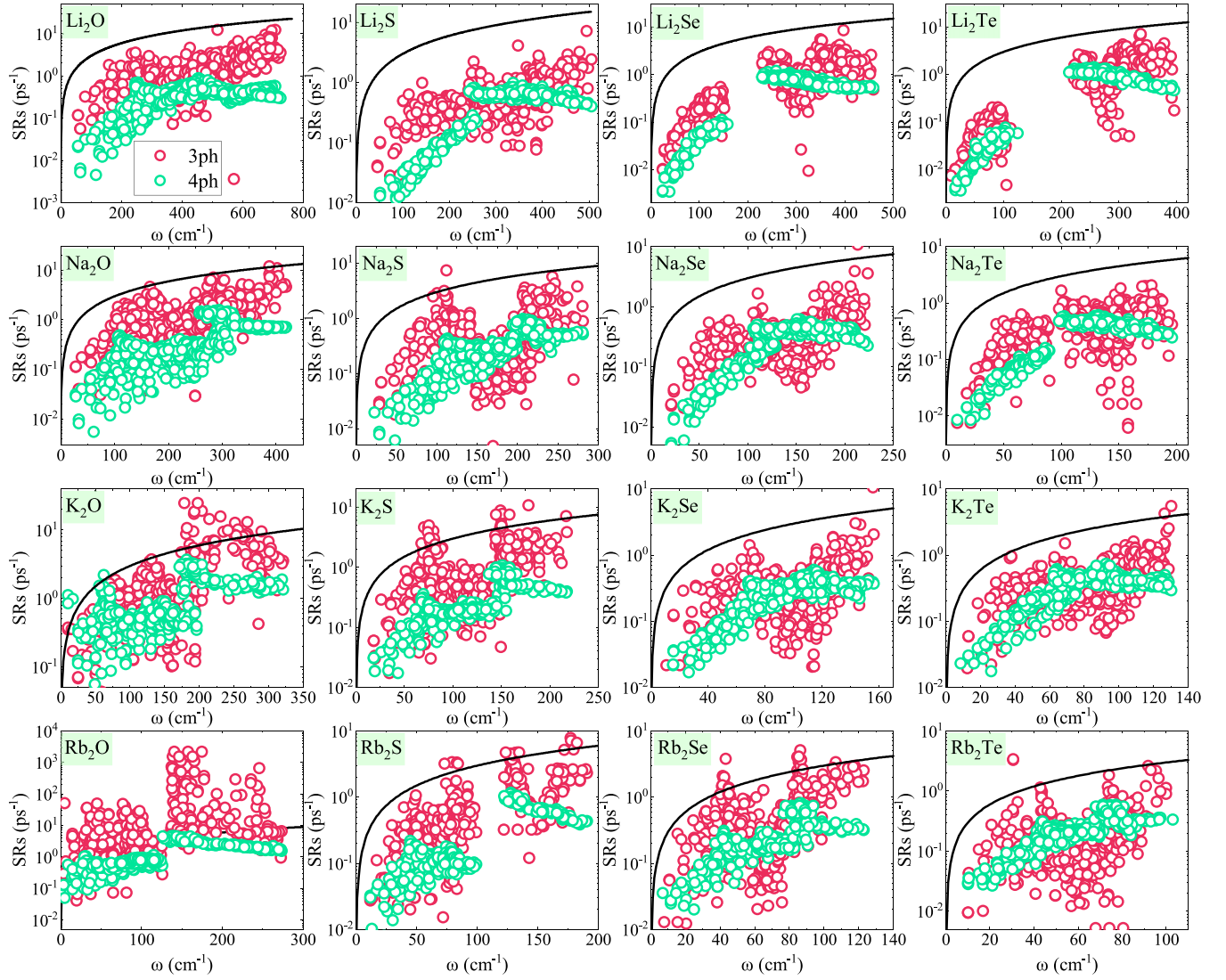


FIG. 11. 3ph and 4ph scattering rates for 16 materials. The black curve in the figure indicates that SRs is equal to the phonon frequency, that is, $1/\tau = \omega/2\pi$.

TABLE II. Calculated elastic constants C_{ij} (in GPa), as well as the bulk modulus B (in GPa), shear modulus G (in GPa), Young's modulus Y (in GPa), and Poisson's ratio ν of 16 inverse fluorite materials. Some experimental values are given as a control.

Material	K ₂ Se	K ₂ Te	Rb ₂ Se	Rb ₂ Te	Cs ₂ Te	Na ₂ Se	Na ₂ Te	Na ₂ S
C_{11}	29.09	22.74	24.96	19.71	16.67	45.01	33.59	54.69/81 (at 30 K) [94]
C_{12}	9.35	8.28	8.18	7.33	6.53	14.03	12.44	15.73/33 (at 30 K) [94]
C_{44}	7.65	6.53	5.78	5.12	3.65	15.11	11.98	17.77/21 (at 30 K) [94]
B_0	15.93	13.10	13.77	11.45	9.91	24.36	19.48	28.72/49 (at 15 K) [95]
G	8.47	6.80	6.72	5.52	4.17	15.26	11.40	18.44
Y	21.91	17.4	17.33	14.27	10.96	37.86	28.62	45.56
ν	0.27	0.28	0.29	0.29	0.32	0.24	0.26	0.24
Material	Rb ₂ S	Li ₂ S	Li ₂ Te	Li ₂ Se	K ₂ S	Na ₂ O	K ₂ O	Li ₂ O
C_{11}	54.69	83.93/95.4 [94]	46.47	66.21	34.32	107.20	63.46	201.64/202 [22]
C_{12}	15.73	18.86/20.9 [94]	15.61	17.16	10.48	18.43	10.47	18.41/21.5 [22]
C_{44}	17.77	33.44	20.89	27.63	8.50	25.68	7.69	55.95
B	28.72	40.55/45.7 [21]	25.90	33.51	18.43	48.02	28.13	79.49/89 [22]
G	18.44	33.08	18.51	26.34	9.74	32.02	12.98	68.14
Y	45.56	78.02	44.84	24.84	24.84	78.60	33.74	159.18
ν	0.24	0.18	0.21	0.19	0.28	0.23	0.30	0.17

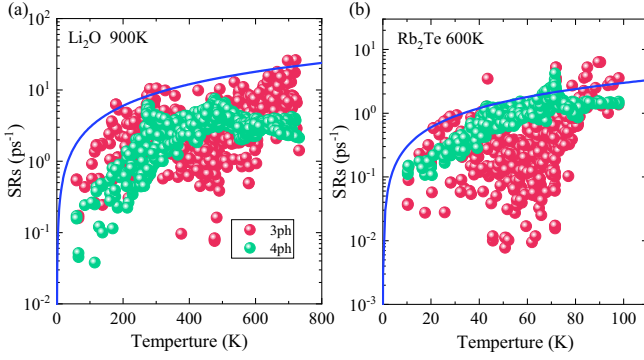


FIG. 12. (a) 3ph and 4ph scattering rates of Li_2O at 900 K. (b) 3ph and 4ph scattering rates of Rb_2Te at 600 K. The blue line is SRs equal to the phonon frequency.

the lattice thermal conductivity is very small, this illustrates the reliability of our calculations.

APPENDIX C: NORMAL AND UMKLAPP SCATTERING PROCESSES OF 16 ANTIFLUORITE MATERIALS AT 300 K

When calculating κ_L , we face a specific question, that is, whether to use an iterative method beyond SMRTA to accurately solve the BTE, to obtain convergence results beyond the SMRTA method, and to obtain convergence results for the phonon normal/Umklapp process [97,98]. If Umklapp dominates and is better than the normal process, then the accuracy of the calculated κ_L is acceptable and there is no need to further use iterative scheme [52]. In our calculations, the iterative method is used to deal with the 3ph process, while the 4ph process is calculated using the SMRTA method. Therefore, it is necessary to check the Umklapp/normal process of 4ph

TABLE III. The calculated lattice thermal conductivity contributed by the off-diagonal terms κ_c , the total lattice thermal conductivity κ_L , and the ratio of κ_c to the total κ_L .

Material	κ_c ($\text{Wm}^{-1}\text{K}^{-1}$)	κ_L ($\text{Wm}^{-1}\text{K}^{-1}$)	Ratio
Li_2O	0.0911	22.3854	0.41%
Li_2S	0.0086	11.9619	0.07%
Li_2Se	0.0477	7.7245	0.61%
Li_2Te	0.0108	5.6121	0.19%
Na_2O	0.1234	8.2026	1.50%
Na_2S	0.0890	4.5876	1.94%
Na_2Se	0.0331	3.3216	0.99%
Na_2Te	0.0244	1.9154	1.27%
K_2O	0.0519	3.3773	1.53%
K_2S	0.0550	2.2834	2.40%
K_2Se	0.0052	2.5455	0.20%
K_2Te	0.0051	1.1072	0.46%
Rb_2O	0.0269	0.0269	1.32%
Rb_2S	0.0272	0.0272	1.44%
Rb_2Se	0.0234	0.0234	2.24%
Rb_2Te	0.0085	1.6104	0.53%

scattering to verify the reasonableness of the calculated κ_L . We plotted the normal and Umklapp processes of 4ph scattering of materials for 16 reactions as shown in Fig. 13. The inset shows the ratio relationship of the Umklapp/normal process at 300 K. It can be found that the Umklapp process in the 16 antifluorite materials is better than the normal process, and the ratio relationship of Umklapp/normal mostly exceeds 1. These phenomena all justify the application of the SMRTA scheme to deal with 4ph scattering processes in 16 selected materials.

APPENDIX D: CONTRIBUTION OF OFF-DIAGONAL TERMS TO LATTICE THERMAL CONDUCTIVITY CALCULATED BY AIAMODE AT 300 K

In addition, if the off-diagonal term of the heat flow operator is considered, which describes the tunneling effect of coherent phonons, the additional contribution κ_c of the lattice thermal conductivity needs to be considered [99–101]. Normally, κ_c is often ignored in simple crystals because the phonon dispersion is well separated and slightly expanded with temperature changes. However, in disordered and glassy amorphous compounds, κ_c may dominate because the phonon and associated group velocities cannot be clearly defined and heat transfer is mediated by diffusions and localizers [102–104]. In our heat transport calculations, only the diagonal term of the heat flow operator is considered. In order to clarify the contribution of off-diagonal terms, we used the ALAMODE software package to calculate κ_c and κ_L of 16 antifluorite structures at 300 K, and provided data on the proportion of κ_c , as shown in Table III. The coherent component of the lattice thermal conductivity is related to the off-diagonal component of the simple harmonic heat flux operator and is calculated as

$$\kappa_c = \frac{1}{NV} \sum_{\mathbf{q}j'} \frac{c_{\mathbf{q}j'}\omega_{\mathbf{q}j'} + c_{\mathbf{q}j}\omega_{\mathbf{q}j}}{\omega_{\mathbf{q}j} + \omega_{\mathbf{q}j'}} v_{\mathbf{q}j} v_{\mathbf{q}j'} \otimes v_{\mathbf{q}j'} \frac{\Gamma_{\mathbf{q}j} + \Gamma_{\mathbf{q}j'}}{(\omega_{\mathbf{q}j} - \omega_{\mathbf{q}j'})^2 + (\Gamma_{\mathbf{q}j} + \Gamma_{\mathbf{q}j'})^2} \quad (\text{D1})$$

where, $c_{\mathbf{q}j}$ represents the mode-specific heat associated with wavevector \mathbf{q} and phonon branch j . V is the volume of the unit cell, $\omega_{\mathbf{q}j}$ is the frequency of the phonon, $\Gamma_{\mathbf{q}j}$ is the phonon linewidth, and $v_{\mathbf{q}}$ is the phonon group velocity. Off-diagonal terms ($j \neq j'$) make coherence contributions. From the data we have given, we can see that the contribution of κ_c to the total κ_L is very small, accounting for less than 2.5%, so it can be ignored.

APPENDIX E: 3,4PH SCATTERING OF 16 ANTIFLUORITE MATERIALS AT 300 K

In order to better understand the calculated differences between selected antifluorite materials and better illustrate the situation of strong 4ph scattering, the SRs of 16 antifluorite materials in the 3ph and 4ph processes at 300 K are plotted as shown in Fig. 11. Overall, the selected reaction is that the material is higher corresponding to 3ph and 4ph is relatively

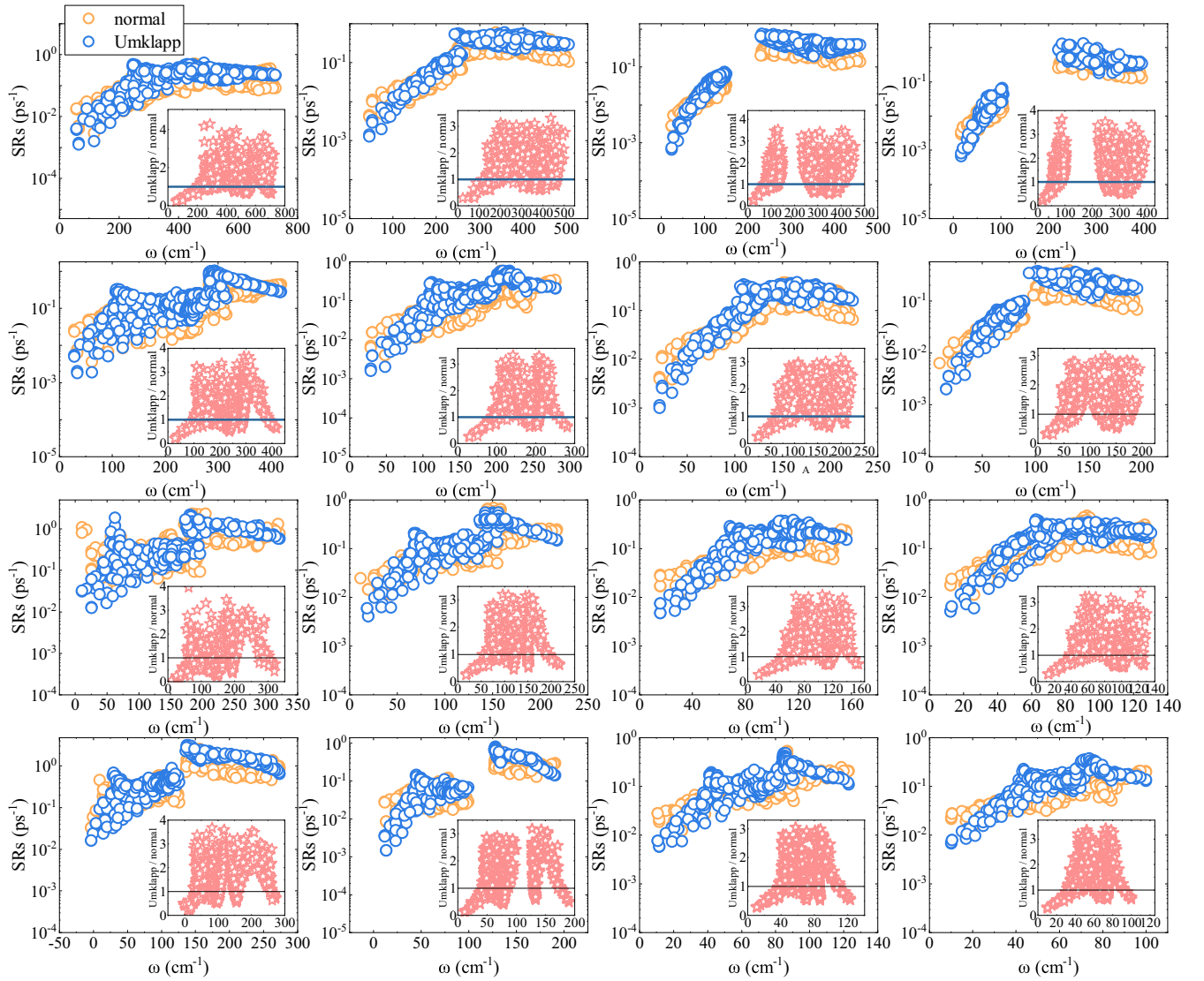


FIG. 13. Dividing 4ph scattering into normal and Umklapp processes at 300 K. The inset shows the ratio of Umklapp and normal processes.

small. Interestingly, the 4ph scattering process of K_2O , Na_2O , K_2Se , and Rb_2S is comparable to the 3ph scattering process at low frequencies, which corresponds to the κ_L ratio shown in Fig. 4, where the κ_L ratio of K_2O , Na_2O , K_2Se , and Rb_2S is less than 0.6. Furthermore, 3ph and 4ph scattering in these materials, except for Rb_2O , are distributed below the curve where SRs equal the phonon frequency, supporting the suitability of phonon quasiparticle images.

APPENDIX F: SCATTERING RATES OF Rb_2Te AND Li_2O AT 600 K AND 900 K RESPECTIVELY

The 3ph and 4ph scattering of Rb_2Te at 600 K and Li_2O at 900 K are shown in Fig. 12. It can be found that as the temperature increases, the 4ph scattering of Li_2O is obviously stronger than that of 3ph. At the same time, the 4ph scattering process of Rb_2O is also comparable to the 3ph scattering process. These results show that the 4ph scattering process can be comparable to or even exceed the 3ph scattering process, showing the importance of 4ph scattering in

the calculation of κ_L . In addition, even though 3ph and 4ph scattering are enhanced due to the increase in temperature, they are still distributed under the curve where SRs are equal to the phonon frequency, so the phonon quasiparticle image is still valid.

APPENDIX G: 3,4PH SCATTERING PHASE SPACE AND DECOMPOSED 4PH SCATTERING PHASE SPACE OF Rb_2Te AND Li_2O AT ROOM TEMPERATURE

Figures 8(b) and 8(e) plot the 3ph and 4ph scattering phase spaces (P_3 and P_4) of Li_2O and Rb_2Te at 300 K. It can be found that P_4 of Li_2O is almost the same as P_3 , and P_4 of Rb_2Te is even exceeding P_3 , this can also explain the strong 4ph scattering contained in Rb_2Te . In addition, P_4 is decomposed into a phase space composed of three separate processes, namely: splitting ($\lambda \rightarrow \lambda_1 + \lambda_2 + \lambda_3$), redistribution ($\lambda + \lambda_1 \rightarrow \lambda_2 + \lambda_3$), and recombination ($\lambda + \lambda_1 + \lambda_2 \rightarrow \lambda_3$) processes, as shown in Figs. 9(c) and 9(f). Taking into account the constraints of phonon energy conservation during

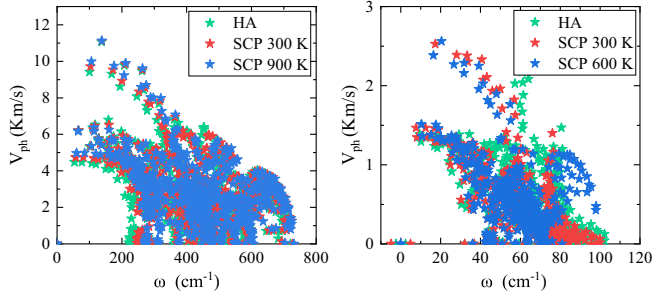


FIG. 14. The phonon group velocity v of Li_2O and Rb_2Te . The results of Li_2O in HA and SCP at 300 K and 900 K and the results of Rb_2Te in HA and SCP at 300 K and 600 K are shown.

scattering, it is expected that the splitting process is mainly related to high-frequency phonon modes, while the recombination process is more relevant to low-frequency phonons. At the same time, more 4ph scattering events result because the redistribution process is more flexible in satisfying phonon

energy conservation. Therefore, it can be concluded that P_4 and 4ph scattering are mainly dominated by the redistribution process, as shown in Figs. 9(c), 9(f), 7(c), and 7(d). At the same time, low-frequency phonons have a considerable recombination process, while high-frequency phonons have a large splitting process, which indicates compliance with the constraints of the law of energy conservation.

APPENDIX H: GROUP VELOCITIES OF 16 ANTIFLUORITE MATERIALS IN HA AND SCP APPROXIMATIONS AT ROOM TEMPERATURE

When exploring the physical mechanism of κ_L , the phonon $v_{q,j}$ is also an important physical quantity. To reveal the calculated differences between Li_2O and Rb_2Te , we first plot the phonon group velocity versus frequency $\omega_{q,j}$ for the two materials in Fig. 14, which shows the SCP results for Li_2O and Rb_2Te at HA and at 300 K, and SCP results at 900 K and 600 K respectively. Observing from the figure, we find that the quartic anharmonic renormalization mainly affects

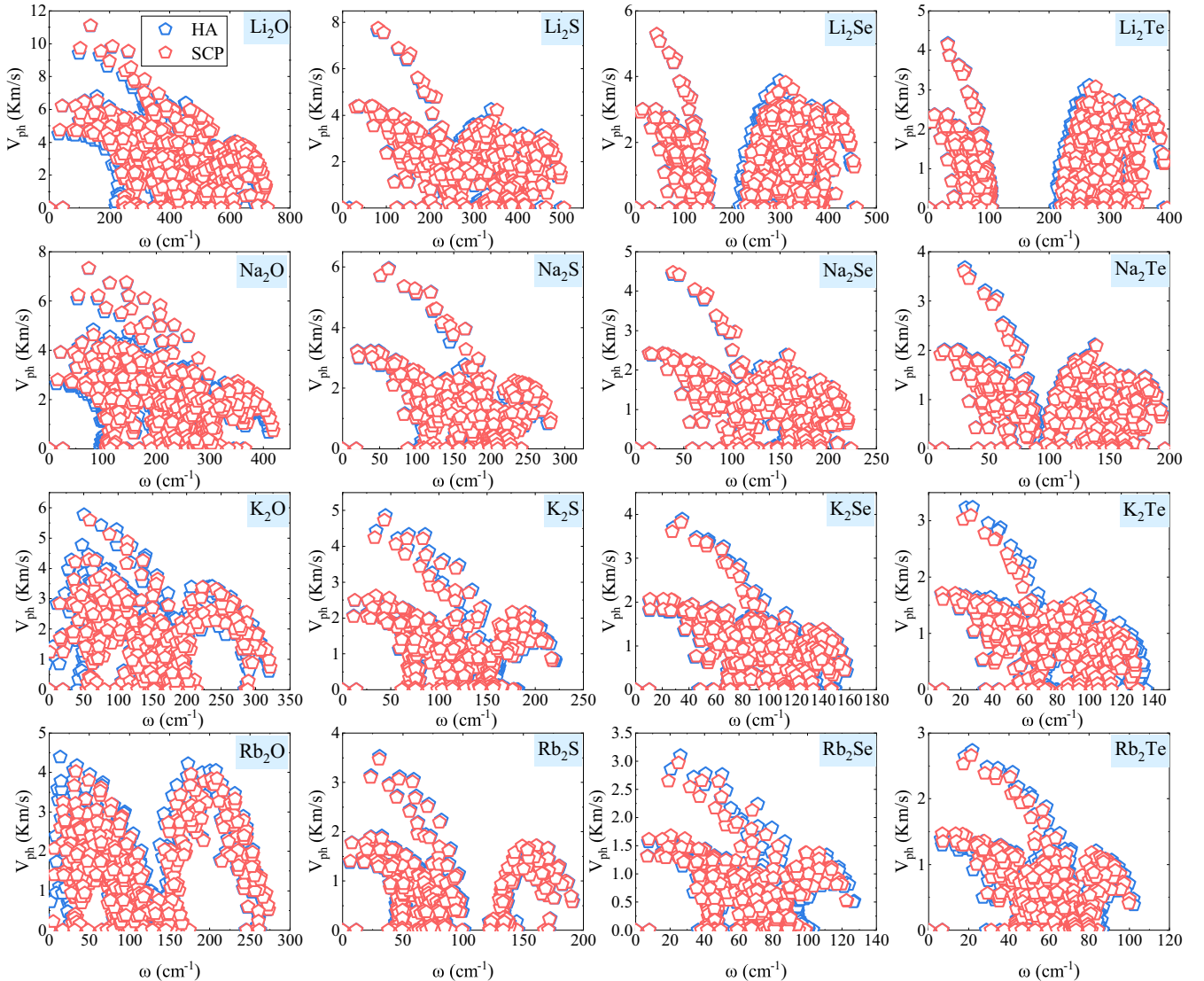


FIG. 15. HA and SCP phonon group velocities $v_{q,j}$ of 16 antifluorite materials at 300 K.

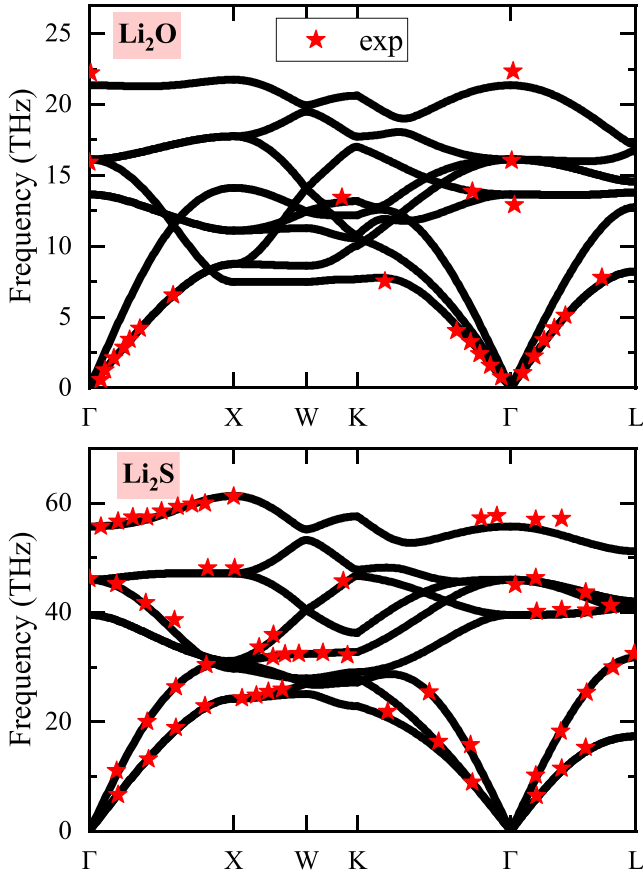


FIG. 16. The black line is the calculated phonon dispersion curve of Li_2O and Li_2S . Experimental data are represented by red five-pointed stars in the figure.

the phonon frequency, which can be attributed to the constant volume specific heat C_v . At the same time, the $v_{q,j}$ is slightly enhanced within a certain frequency range. In addition, it can be seen from Fig. 14 that as the temperature increases, the frequency of Li_2O continues to increase, while the frequency of Rb_2O increases at low frequencies and decreases at high temperatures. This is consistent with the acoustic properties of these two materials. The subspectrum situations are exactly the same, as shown in Figs. 5(a) and 5(d).

Subsequently, the $v_{q,j}$ of 16 antiferroite materials under HA results and SCP results at 300 K are shown in Fig. 15 to understand the differences in κ_L of the selected antiferroite materials. It can be found from the figure that the quartic anharmonic renormalization only slightly increases or decreases the group velocity under SCP, which shows that the main influence is their phonon frequency. In addition, in addition to strong 3ph and 4ph scattering, materials with very small κ_L , such as $\kappa_{3,4\text{ph}}^{\text{SCP}} < 3.0 \text{ W/mK}$, have relatively small $v_{q,j}$ of low-frequency phonons, such as cubic $\text{Rb}_2\text{Te/S/Se}$ and K_2S in Fig. 17 are shown.

APPENDIX I: CONSTANT-VOLUME SPECIFIC HEAT C_v FOR 16 ANTIFLOURITE MATERIALS

According to Eq. (1), we know that in addition to the total SRs and phonon group velocity, the factors that affect

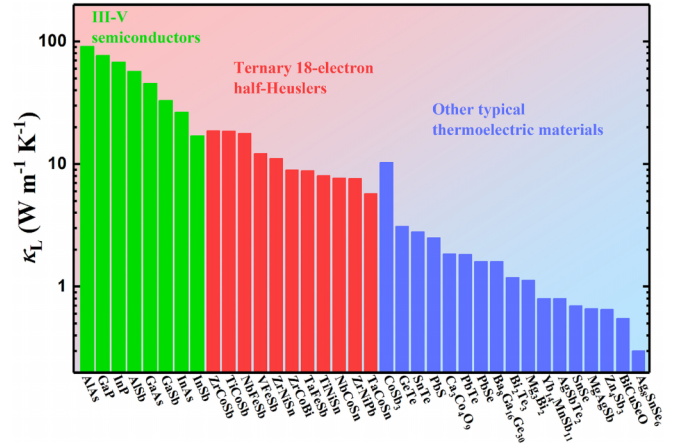


FIG. 17. Comparison of lattice thermal conductivity (κ_L) at room temperature of III-V semiconductors, ternary 18-electron half-Heusler semiconductors and other typical thermoelectric materials [87–92].

κ_L include constant volume specific heat C_v . Therefore, we plotted the C_v of 16 materials in Fig. 18. It can be seen that Li_2O has the largest C_v , while Rb_2O has the largest C_v , and the gap is very large. This shows that C_v is also an important reason affecting the κ_L gap and cannot be ignored.

APPENDIX J: CONSIDER THE IMPACT OF THE SELF-ENERGY SECOND-ORDER MODIFIED BUBBLE TERM ON PHONON RENORMALIZATION

In highly anharmonic crystalline compounds, the thermal or quantum fluctuations of atoms are too pronounced for the quasiharmonic phonon theory to accurately evaluate the lattice dynamics [105]. These factors are crucial in determining thermal conductivity and its dependence on temperature, as they control the pattern of phonon transport and interaction within the crystal framework [106,107]. With the development of the phonon self-consistent theory based on the quasiparticle approximation (QP), the accurate modeling of anharmonic lattice dynamics at finite temperature has been achieved by introducing the effective single body Hamiltonian of interacting phonons [108,109].

To describe the intrinsic scattering process of phonons and the temperature dependence of phonon frequency, it is necessary to consider anharmonic terms, which appear as interactions between harmonic (noninteracting) phonons. This relationship can be expressed using Dyson's formula,

$$\{G_q(\omega)\}^{-1} = \{G_0^q(\omega)\} - \Sigma_q[G](\omega) \quad (\text{J1})$$

where $G_{qj}^0(\omega)$ is the noninteracting phonon propagator and $\Sigma_q[G](\omega)$ is the anharmonic self-energy. For self-energy, the most important terms usually considered are those related to cubic and quartic anharmonicities, which can be expressed as

$$\Sigma_q[G](\omega) = \Sigma_q^T[G, \Phi_3] + \Sigma_q^L[G, \Phi_4] + \Sigma_q^B[G, \Phi_3](\omega) \quad (\text{J2})$$

where, T, L, and B are tadpole, loop and bubble diagrams, respectively. Their dependence on anharmonic force constants (Φ_3, Φ_4) is indicated explicitly. Among them, tadpole and

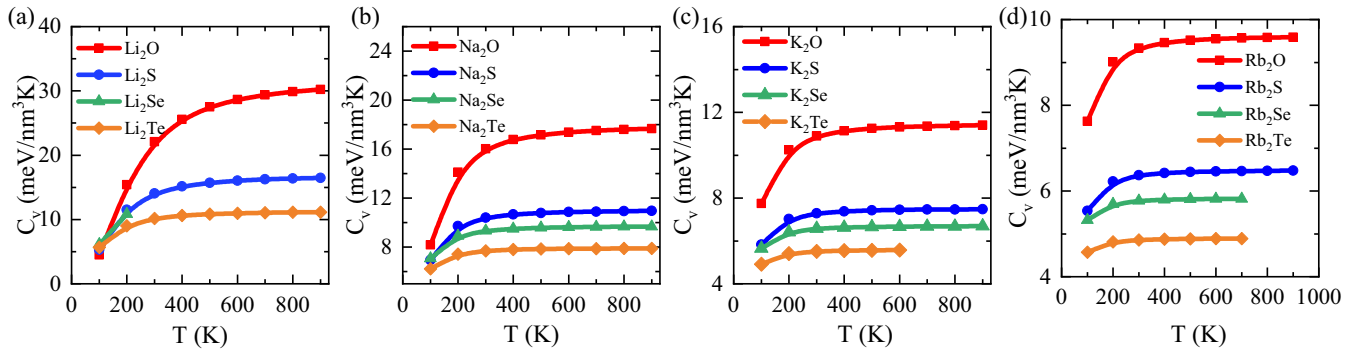


FIG. 18. Constant-volume specific heat C_v for 16 cubic antiferroite (a) Li_2O , Li_2S , Li_2Se , Li_2Te , (b) Na_2O , Na_2S , Na_2Se , Na_2Te , (c) K_2O , K_2S , K_2Se , K_2Te , and (d) Rb_2O , Rb_2S , Rb_2Se , Rb_2Te .

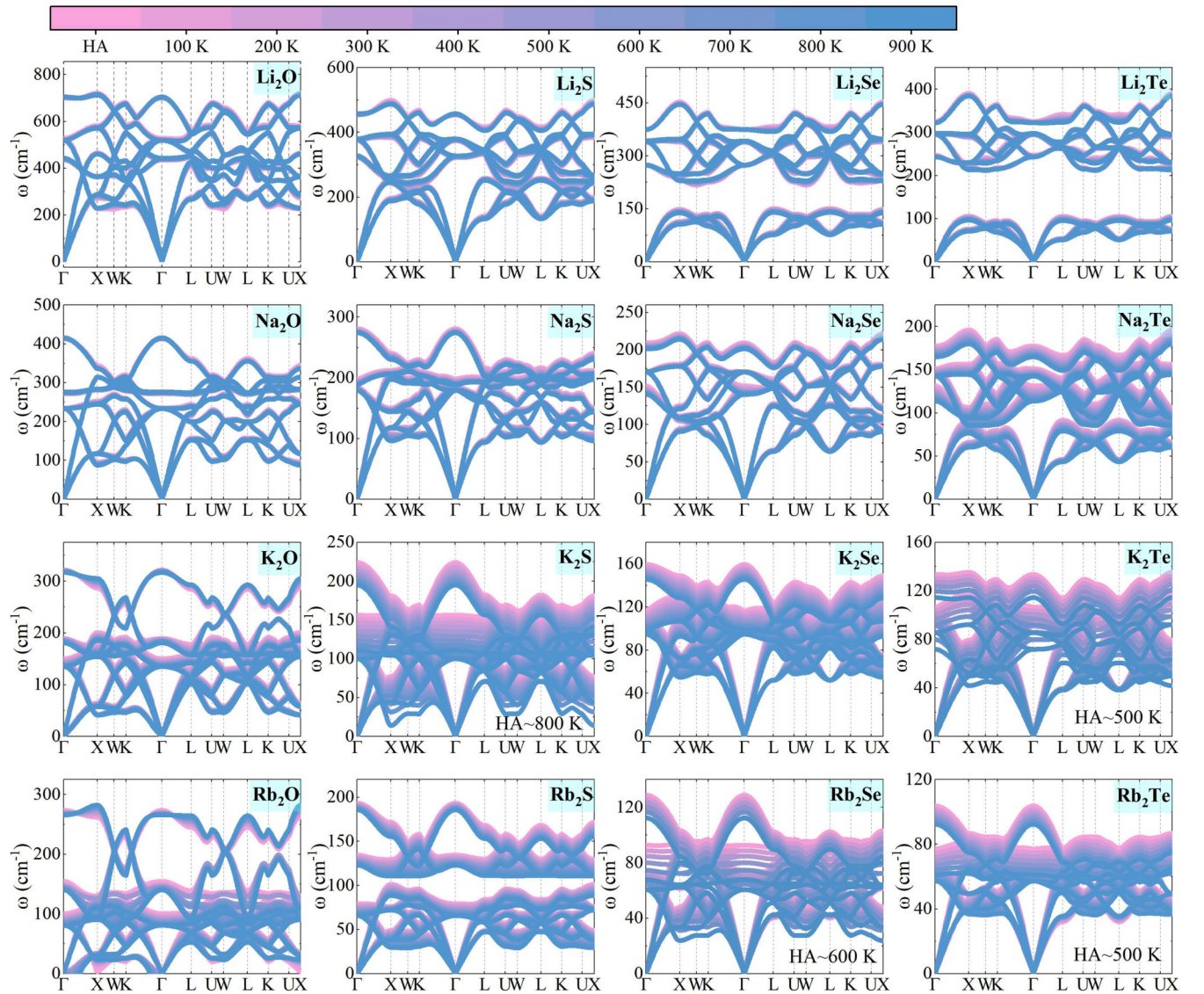


FIG. 19. The phonon dispersion curves of 16 antiferroite materials calculated under the SCPB + 3, 4ph method as the temperature changes are a, Li_2O , Li_2S , Li_2Se , Li_2Te , Na_2O , Na_2S , Na_2Se , Na_2Te , K_2O , K_2S , K_2Se , K_2Te , Rb_2O , Rb_2S , Rb_2Se , Rb_2Te , HA are 0 K. Except K_2Te and Rb_2Te are considered at 500 K, Rb_2Se is considered at 600 K, and K_2S is considered at 800 K. Except for this, other materials are considered at 900 K.

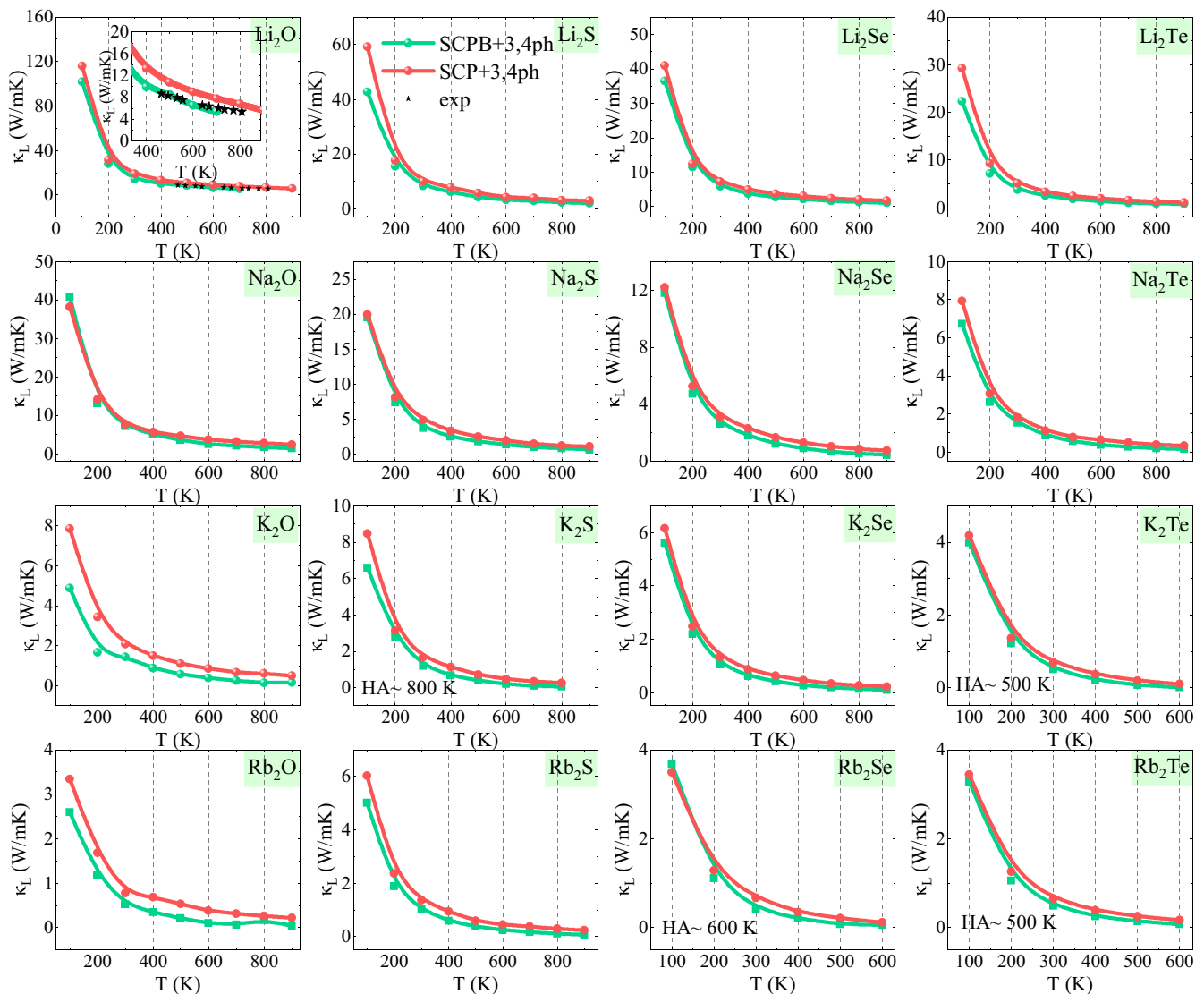


FIG. 20. The lattice thermal conductivities of 16 antiferroelectric materials calculated under the SCP + 3,4ph and SCPB + 3,4ph methods. Triangles in Li_2O give comparison of experimental values.

loop diagrams are real numbers, while bubble and 4ph diagrams are frequency-dependent complex numbers. Therefore, the bubble diagrams and the 4ph diagrams contribute to the linewidth of the phonons. The SCP + bubble (SCPB) theory has recently been proposed to consider B in SCP theory. Therefore, based on our calculation results, we consider the renormalization of the phonon spectrum by the bubble diagrams and fully consider the impact of anharmonicity.

In order to study the influence of the bubble term on phonon renormalization, we considered the impact of the cubic anharmonicity on the basis of the first-order modified SCP + 3, 4ph relative to the quartic anharmonicity, denoted as SCPB + 3,4ph. It is important to note the importance of cubic and quartic interatomic force constants in accurately predicting lattice dynamics within materials that exhibit strong anharmonicity [110]. In general, the frequency shift induced by anharmonicity at finite temperatures is represented by the real part of the phonon self-energy [47,111]. Specifically, considering the first-order correction due to quartic

anharmonicity, the SCP method typically yields a positive contribution to the phonon frequency. However, SCP theory tends to overestimate phonon frequencies, primarily due to the neglect of the negative frequency shift associated with the bubble self-energy [112]. By incorporating the second-order correction from cubic anharmonicity, we compared the phonon dispersion curves obtained using the HA method and the SCPB method at 0 K and various temperatures, as shown in Fig. 19. Obviously, at low frequencies, the hardening effect of the phonon spectrum under the SCP theory weakens. For the seven materials Na_2Te , $\text{K}_2\text{S/Se/Te}$, and $\text{Rb}_2\text{S/Se/Te}$, the high-frequency optical branch behaves as the temperature increases. It is worth noting, however, that the high-frequency optical branch of these materials contributes less to the κ_L . The displacement associated with the bubble diagrams does not have a significant influence in the system we studied. However, in some systems, the frequency shift associated with the neglected bubble diagrams is substantial; for instance, it is particularly large in $\alpha\text{-CuPbBr}_3$. The competitive

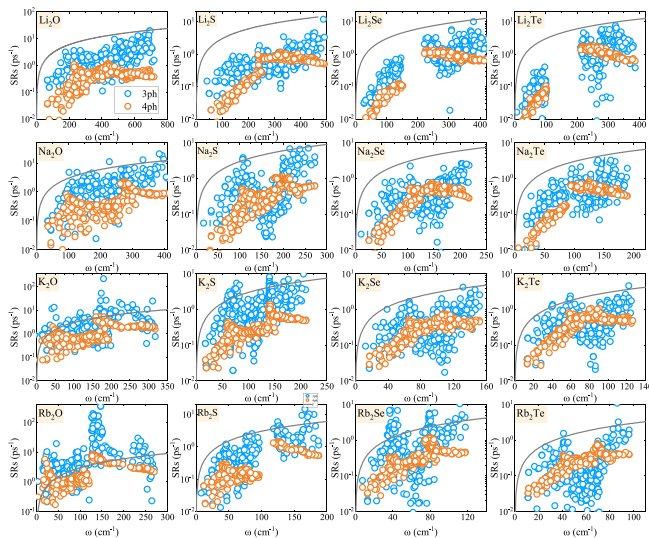


FIG. 21. Calculated 3ph and 4ph scattering rates for 16 materials using SCPB + 3,4ph at 300 K. The gray curve indicates that SRs is equal to the phonon frequency, that is, $1/\tau = \omega/2\pi$.

relationship between the phonon hardening described by the loop diagrams and the softening caused by the bubble diagrams has a decisive impact on the propagation of particles. This effect is significant in materials with strong anharmonicity, and the contribution of the bubble term cannot be ignored [49]. Conversely, in some other materials, this contribution can be disregarded.

Next, we explored the impact of anharmonic lattice dynamics on thermal conductivity in depth. In Fig. 20, we plotted the κ_L for 16 antiferroelectric materials using SCP + 3,4ph and SCPB + 3,4ph methods. It can be observed that in our studied system, the impact of including the bubble diagrams is not very significant. Compared to the κ_L obtained by the first-order correction SCP + 3,4ph for quartic anharmonicity, the κ_L obtained by SCPB + 3,4ph, which includes the influence of cubic anharmonicity, is reduced. For Li_2O , the κ_L value obtained by SCPB + 3,4ph aligns better with the

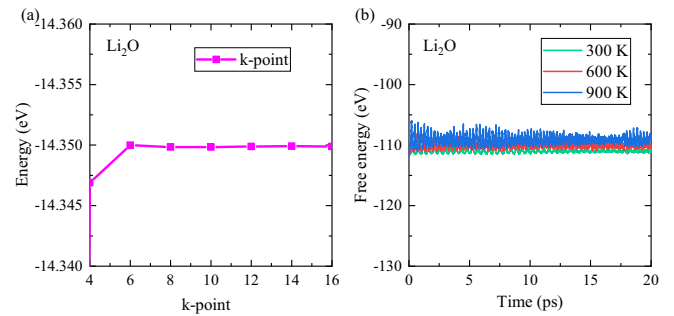


FIG. 22. (a) Convergence test of k-point grid for Li_2O . (b) Calculated AIMD simulation of Li_2O . Green, red, and blue represent 300 K, 600 K, and 900 K respectively.

experimental values, demonstrating that our calculation method is comprehensive and verifies the accuracy of our approach. To further elucidate the thermal transport characteristics, Fig. 21 shows the 3ph and 4ph scattering rates of 16 materials under the SCPB + 3,4ph method at 300 K. Except for Rb_2O , the 3ph and 4ph scattering distributions of the other materials are below the $1/\tau = \omega/2\pi$ curve, supporting the validity of the BTE solution presented in this article.

APPENDIX K: K-POINT GRID TEST AND THERMAL STABILITY TEST OF Li_2O

The k-point grid controls the parameters of the Brillouin zone integration and plays a huge role in obtaining accurate results. Calculation accuracy can usually be improved by increasing the number of points. However, the larger the number of irreducible k points, the higher the computational cost. In this article, taking Li_2O as an example, the k-point grid used in the calculation is $12 \times 12 \times 12$. In order to ensure the accuracy of our calculations, we conducted a convergence test on the k-point grid, as shown in Fig. 22(a). It shows that when the k-point grid reaches $8 \times 8 \times 8$, convergence has been achieved, so the k-point grid we chose is $12 \times 12 \times 12$.

- [1] K. Esfarjani, G. Chen, and H. T. Stokes, Heat transport in silicon from first-principles calculations, *Phys. Rev. B* **84**, 085204 (2011).
- [2] S. Mukhopadhyay and D. A. Stewart, Polar effects on the thermal conductivity of cubic boron nitride under pressure, *Phys. Rev. Lett.* **113**, 025901 (2014).
- [3] D. A. Broido, M. Malorny, G. Birner, N. Mingo, and D. A. Stewart, Intrinsic lattice thermal conductivity of semiconductors from first principles, *Appl. Phys. Lett.* **91**, 231922 (2007).
- [4] A. J. Minnich, J. A. Johnson, A. J. Schmidt, K. Esfarjani, M. S. Dresselhaus, K. A. Nelson, and G. Chen, Thermal conductivity spectroscopy technique to measure phonon mean free paths, *Phys. Rev. Lett.* **107**, 095901 (2011).
- [5] Y. K. Koh and D. G. Cahill, Frequency dependence of the thermal conductivity of semiconductor alloys, *Phys. Rev. B* **76**, 075207 (2007).
- [6] F. Yang and C. Dames, Mean free path spectra as a tool to understand thermal conductivity in bulk and nanostructures, *Phys. Rev. B* **87**, 035437 (2013).
- [7] L. E. Bell, Cooling, heating, generating power, and recovering waste heat with thermoelectric systems, *Science* **321**, 1457 (2008).
- [8] M. Dutta, D. Sarkar, and K. Biswas, Intrinsically ultralow thermal conductive inorganic solids for high thermoelectric performance, *Chem. Commun.* **57**, 4751 (2021).
- [9] G. A. Slack, Thermal conductivity of pure and impure silicon, silicon carbide, and diamond, *J. Appl. Phys.* **35**, 3460 (1964).
- [10] M. Huang, P. Eames, B. Norton, and N. Hewitt, Natural convection in an internally finned phase change material heat sink for the thermal management of photovoltaics, *Sol. Energy Mater. Sol. Cells* **95**, 1598 (2011).
- [11] X. Lou, S. Li, X. Chen, Q. Zhang, H. Deng, J. Zhang, D. Li, X. Zhang, Y. Zhang, H. Zeng, and G. Tang, Lattice strain leads to

- high thermoelectric performance in polycrystalline SnSe, *ACS Nano* **15**, 8204 (2021).
- [12] M. Hong, Z.-G. Chen, L. Yang, T. C. Chasapis, S. D. Kang, Y. Zou, G. J. Auchtung, M. G. Kanatzidis, G. J. Snyder, and J. Zou, Enhancing the thermoelectric performance of $\text{SnSe}_{1-x}\text{Te}_x$ nanoplates through band engineering, *J. Mater. Chem. A* **5**, 10713 (2017).
- [13] L. D. Zhao, D. Berardan, Y. L. Pei, C. Byl, L. Pinsard-Gaudart, and N. Dragoe, $\text{Bi}_{1-x}\text{Sr}_x\text{CuSeO}$ oxyselenides as promising thermoelectric materials, *Appl. Phys. Lett.* **97**, 092118 (2010).
- [14] A. Piccioli, R. Pegna, I. Fedorko, M. Giunta, N. Malakhov, A. Menzione, F. Raffaelli, A. Braem, E. Chesi, C. Joram, J. Séuïno, G. Sartori, and P. Weilhammer, Characterization of a potted 5-in. HPD with Rb_2Te photocathode, *Nucl. Instrum. Methods Phys. Res. Sect. A* **518**, 602 (2004).
- [15] C. Joram, Large area hybrid photodiodes, *Nucl. Phys. B* **78**, 407 (1999).
- [16] D. Bisero, A. di Bona, P. Paradisi, and S. Valeri, K_2Te photocathode growth: A photoemission study, *J. Appl. Phys.* **87**, 543 (2000).
- [17] R. Ali, R. Khanata, B. Amin, G. Murtaza, and S. B. Omran, Structural, elastic, electronic, chemical bonding and optical properties of $M_2\text{Se}$ ($M = \text{Li, Na, K, Rb}$) through first principle study, *Int. J. Mod. Phys. B* **27**, 1350170 (2013).
- [18] H. Kikuchi, H. Iyetomi, and A. Hasegawa, Insight into the origin of superionic conductivity from electronic structure theory, *J. Phys.: Condens. Matter* **10**, 11439 (1998).
- [19] X. Zhang, C. Ying, H. Ma, G. Shi, and Z. Li, First principles study on lattice dynamics, thermodynamics and elastic properties of Na_2Te under high pressure, *Phys. Scr.* **88**, 035602 (2013).
- [20] K. Seifert-Lorenz and J. Hafner, Crystalline intermetallic compounds in the K-Te system: The Zintl-Klemm principle revisited, *Phys. Rev. B* **66**, 094105 (2002).
- [21] W. Buehrer, F. Altorfer, J. Mesot, H. Bill, P. Carron, and H. G. Smith, Lattice dynamics and the diffuse phase transition of lithium sulphide investigated by coherent neutron scattering, *J. Phys.: Condens. Matter* **3**, 1055 (1991).
- [22] S. Hull, T. Farley, W. Hayes, and M. Hutchings, The elastic properties of lithium oxide and their variation with temperature, *J. Nucl. Mater.* **160**, 125 (1988).
- [23] G. D. Mahan, Exactly solvable models, *Many-Particle Physics* (Springer, Boston, MA, 2000), pp. 187–294.
- [24] R. Kubo, M. Toda, and N. Hashitsume, *Statistical Physics II: Nonequilibrium Statistical Mechanics*, Springer Series in Solid-State Sciences, Vol. 31 (Springer, Berlin, Heidelberg, 2012).
- [25] A. Ward, D. A. Broido, D. A. Stewart, and G. Deinzer, *Ab initio* theory of the lattice thermal conductivity in diamond, *Phys. Rev. B* **80**, 125203 (2009).
- [26] A. Togo, L. Chaput, and I. Tanaka, Distributions of phonon lifetimes in Brillouin zones, *Phys. Rev. B* **91**, 094306 (2015).
- [27] P. C. Trivedi, H. O. Sharma, and L. S. Kothari, Lattice anharmonicity of alkali metals, *Phys. Rev. B* **18**, 2668 (1978).
- [28] X. Chen, C. Li, F. Tian, G. A. Gamage, S. Sullivan, J. Zhou, D. Broido, Z. Ren, and L. Shi, Thermal expansion coefficient and lattice anharmonicity of cubic boron arsenide, *Phys. Rev. Appl.* **11**, 064070 (2019).
- [29] S. Zeng, L. Fang, Y. Tu, M. Zulfiqar, and G. Li, Ultralow lattice thermal conductivity of binary compounds A_2B ($A = \text{Cs, Rb}$ and $B = \text{Se, Te}$) with higher-order anharmonicity correction, *Phys. Chem. Chem. Phys.* **25**, 12157 (2023).
- [30] Y. Xia, V. I. Hegde, K. Pal, X. Hua, D. Gaines, S. Patel, J. He, M. Aykol, and C. Wolverton, High-throughput study of lattice thermal conductivity in binary rocksalt and zinc blende compounds including higher-order anharmonicity, *Phys. Rev. X* **10**, 041029 (2020).
- [31] Y. Zhao, S. Zeng, G. Li, C. Lian, Z. Dai, S. Meng, and J. Ni, Lattice thermal conductivity including phonon frequency shifts and scattering rates induced by quartic anharmonicity in cubic oxide and fluoride perovskites, *Phys. Rev. B* **104**, 224304 (2021).
- [32] N. R. Werthamer, Self-consistent phonon formulation of anharmonic lattice dynamics, *Phys. Rev. B* **1**, 572 (1970).
- [33] I. Errea, M. Calandra, and F. Mauri, First-principles theory of anharmonicity and the inverse isotope effect in superconducting palladium-hydride compounds, *Phys. Rev. Lett.* **111**, 177002 (2013).
- [34] P. Souvatzis, O. Eriksson, M. I. Katsnelson, and S. P. Rudin, Entropy driven stabilization of energetically unstable crystal structures explained from first principles theory, *Phys. Rev. Lett.* **100**, 095901 (2008).
- [35] O. Hellman and I. A. Abrikosov, Temperature-dependent effective third-order interatomic force constants from first principles, *Phys. Rev. B* **88**, 144301 (2013).
- [36] O. Hellman, I. A. Abrikosov, and S. I. Simak, Lattice dynamics of anharmonic solids from first principles, *Phys. Rev. B* **84**, 180301(R) (2011).
- [37] A. Gulans, S. Kontur, C. Meisenbichler, D. Nabok, P. Pavone, S. Rigamonti, S. Sagmeister, U. Werner, and C. Draxl, exciting: A full-potential all-electron package implementing density-functional theory and many-body perturbation theory, *J. Phys.: Condens. Matter* **26**, 363202 (2014).
- [38] O. Hellman, P. Steneteg, I. A. Abrikosov, and S. I. Simak, Temperature dependent effective potential method for accurate free energy calculations of solids, *Phys. Rev. B* **87**, 104111 (2013).
- [39] F. Zhou, W. Nielson, Y. Xia, and V. Ozoliņš, Lattice anharmonicity and thermal conductivity from compressive sensing of first-principles calculations, *Phys. Rev. Lett.* **113**, 185501 (2014).
- [40] F. Zhou, B. Sadigh, D. Åberg, Y. Xia, and V. Ozoliņš, Compressive sensing lattice dynamics. II. Efficient phonon calculations and long-range interactions, *Phys. Rev. B* **100**, 184309 (2019).
- [41] F. Zhou, W. Nielson, Y. Xia, and V. Ozoliņš, Compressive sensing lattice dynamics. I. General formalism, *Phys. Rev. B* **100**, 184308 (2019).
- [42] K. Shukla, A. Paskin, D. O. Welch, and G. J. Dienes, Self-consistent-average-phonon equation of state. Formalism and comparison with self-consistent-phonon calculations, *Phys. Rev. B* **24**, 724 (1981).
- [43] R. Masuki, T. Nomoto, R. Arita, and T. Tadano, Anharmonic Grüneisen theory based on self-consistent phonon theory: Impact of phonon-phonon interactions neglected in the quasi-harmonic theory, *Phys. Rev. B* **105**, 064112 (2022).
- [44] S. Adhikari, C. L. Cortes, X. Wen, S. Panuganti, D. J. Gosztola, R. D. Schaller, G. P. Wiederrecht, and S. K. Gray,

- Accelerating ultrafast spectroscopy with compressive sensing, *Phys. Rev. Appl.* **15**, 024032 (2021).
- [45] M. Y. Hu, X. Yong, N. J. English, and J. S. Tse, Onset of anharmonicity and thermal conductivity in SnSe, *Phys. Rev. B* **104**, 184303 (2021).
- [46] X. Yang, T. Feng, J. S. Kang, Y. Hu, J. Li, and X. Ruan, Observation of strong higher-order lattice anharmonicity in Raman and infrared spectra, *Phys. Rev. B* **101**, 161202(R) (2020).
- [47] T. Tadano and S. Tsuneyuki, Self-consistent phonon calculations of lattice dynamical properties in cubic SrTiO₃ with first-principles anharmonic force constants, *Phys. Rev. B* **92**, 054301 (2015).
- [48] A. Debernardi, S. Baroni, and E. Molinari, Anharmonic phonon lifetimes in semiconductors from density-functional perturbation theory, *Phys. Rev. Lett.* **75**, 1819 (1995).
- [49] A. A. Maradudin and A. E. Fein, Scattering of neutrons by an anharmonic crystal, *Phys. Rev.* **128**, 2589 (1962).
- [50] R. A. Cowley, Anharmonic crystals, *Rep. Prog. Phys.* **31**, 123 (1968).
- [51] W. Li, J. Carrete, N. A. Katcho, and N. Mingo, ShengBTE: A solver of the Boltzmann transport equation for phonons, *Comput. Phys. Commun.* **185**, 1747 (2014).
- [52] Z. Han, X. Yang, W. Li, T. Feng, and X. Ruan, Fourphonon: An extension module to ShengBTE for computing four-phonon scattering rates and thermal conductivity, *Comput. Phys. Commun.* **270**, 108179 (2022).
- [53] I. Errea, M. Calandra, and F. Mauri, Anharmonic free energies and phonon dispersions from the stochastic self-consistent harmonic approximation: Application to platinum and palladium hydrides, *Phys. Rev. B* **89**, 064302 (2014).
- [54] I. Errea, B. Rousseau, and A. Bergara, Anharmonic stabilization of the high-pressure simple cubic phase of calcium, *Phys. Rev. Lett.* **106**, 165501 (2011).
- [55] T. R. Koehler, Theory of the self-consistent harmonic approximation with application to solid neon, *Phys. Rev. Lett.* **17**, 89 (1966).
- [56] A. van Roekeghem, J. Carrete, and N. Mingo, Anomalous thermal conductivity and suppression of negative thermal expansion in ScF₃, *Phys. Rev. B* **94**, 020303(R) (2016).
- [57] U. Aseginolaza, R. Bianco, L. Monacelli, L. Paulatto, M. Calandra, F. Mauri, A. Bergara, and I. Errea, Phonon collapse and second-order phase transition in thermoelectric SnSe, *Phys. Rev. Lett.* **122**, 075901 (2019).
- [58] T. Feng and X. Ruan, Quantum mechanical prediction of four-phonon scattering rates and reduced thermal conductivity of solids, *Phys. Rev. B* **93**, 045202 (2016).
- [59] G. Kresse and J. Furthmüller, Efficient iterative schemes for *ab initio* total-energy calculations using a plane-wave basis set, *Phys. Rev. B* **54**, 11169 (1996).
- [60] G. Kresse and D. Joubert, From ultrasoft pseudopotentials to the projector augmented-wave method, *Phys. Rev. B* **59**, 1758 (1999).
- [61] J. P. Perdew, K. Burke, and M. Ernzerhof, Generalized gradient approximation made simple, *Phys. Rev. Lett.* **77**, 3865 (1996).
- [62] T. Tadano, Y. Gohda, and S. Tsuneyuki, Anharmonic force constants extracted from first-principles molecular dynamics: Applications to heat transfer simulations, *J. Phys.: Condens. Matter* **26**, 225402 (2014).
- [63] T. Feng, L. Lindsay, and X. Ruan, Four-phonon scattering significantly reduces intrinsic thermal conductivity of solids, *Phys. Rev. B* **96**, 161201(R) (2017).
- [64] T. Takahashi and T. Kikuchi, Porosity dependence on thermal diffusivity and thermal conductivity of lithium oxide Li₂O from 200 to 900 °C, *J. Nucl. Mater.* **91**, 93 (1980).
- [65] R. Eithiraj, G. Jaiganesh, and G. Kalpana, Electronic structure and ground-state properties of alkali-metal oxides Li₂O, Na₂O, K₂O and Rb₂O: A first-principles study, *Phys. B: Condens. Matter* **396**, 124 (2007).
- [66] K. Bidai, M. Ameri, A. Zaoui, I. Ameri, and Y. Al-Douri, First principle study of mechanical stability and thermodynamic properties of anti-fluorite Li₂O and Rb₂O under pressure and temperature effect, *Chinese J. Phys.* **54**, 678 (2016).
- [67] S. Saib and N. Bouarissa, First-principles investigation of structural, elastic, lattice dynamical and thermodynamic properties of lithium sulfur under pressure, *Mater. Res. Express* **4**, 105901 (2017).
- [68] R. D. Eithiraj, G. Jaiganesh, G. Kalpana, and M. Rajagopalan, First-principles study of electronic structure and ground-state properties of alkali-metal sulfides—Li₂S, Na₂S, K₂S and Rb₂S, *Physica Status Solidi (b)* **244**, 1337 (2007).
- [69] X. Zhang, C. Ying, G. Shi, Z. Li, and H. Shi, A first-principles study on lattice dynamics, thermodynamics and elastic properties of lithium selenide under high pressure, *Comput. Mater. Sci.* **79**, 903 (2013).
- [70] K. Bidai, M. Ameri, I. Ameri, D. Bensaid, A. Slamani, A. Zaoui, and Y. Al-Douri, Structural, mechanical and thermodynamic properties under pressure effect of rubidium telluride: First principle calculations, *Arch. Metall. Mater.* **62**, 865 (2017).
- [71] F. Kalarasse and B. Bennecer, Elastic properties and lattice dynamics of alkali chalcogenide compounds Na₂S, Na₂Se and Na₂Te, *Comput. Mater. Sci.* **50**, 1806 (2011).
- [72] S. M. Alay-e-Abbas, N. Sabir, Y. Saeed, and A. Shaukat, Electronic and optical properties of alkali metal selenides in anti-CaF₂ crystal structure from first-principles, *J. Alloys Compd.* **503**, 10 (2010).
- [73] F.-Y. Xu, D. Wang, Z.-Y. Zeng, Z.-G. Li, X.-R. Chen, and G.-F. Ji, Thermal transport and thermoelectric properties of alkali-metal telluride Na₂Te from first-principles study, *Solid State Commun.* **354**, 114890 (2022).
- [74] A. E. Gheribi, A. Seifitokaldani, P. Wu, and P. Chartrand, An *ab initio* method for the prediction of the lattice thermal transport properties of oxide systems: Case study of Li₂O and K₂O, *J. Appl. Phys.* **118**, 145101 (2015).
- [75] N. Tayebi, K. Bidai, M. Ameri, S. Amel, I. Ameri, Y. Al-Douri, and D. Varshney, Pressure and temperature dependence of the structural, elastic and thermodynamic properties of potassium telluride: First-principles calculations, *Chinese J. Phys.* **55**, 769 (2017).
- [76] Z. Souadia, A. Bouhemadou, R. Khenata, and Y. Al-Douri, Structural, elastic and lattice dynamical properties of the alkali metal tellurides: First-principles study, *Phys. B: Condens. Matter* **521**, 204 (2017).
- [77] S. M. Alay-e-Abbas and A. Shaukat, First principles study of structural, electronic and optical properties of polymorphic forms of Rb₂Te, *Solid State Sci.* **13**, 1052 (2011).

- [78] E. Zintl, A. Harder, and B. Dauth, Gitterstruktur der oxyde, sulfide, selenide und telluride des lithiums, natriums und kaliums, *Z. Elektrochem. Angew. Phys. Chem.* **40**, 588 (1934).
- [79] Z. Tian, J. Garg, K. Esfarjani, T. Shiga, J. Shiomi, and G. Chen, Phonon conduction in PbSe, PbTe, and $\text{PbTe}_{1-x}\text{Se}_x$ from first-principles calculations, *Phys. Rev. B* **85**, 184303 (2012).
- [80] A. El-Sharkawy, A. Abou El-Azm, M. Kenawy, A. Hillaal, and H. Abu-Basha, Thermophysical properties of polycrystalline PbS, PbSe, and PbTe in the temperature range 300–700 K, *Int. J. Thermophys.* **4**, 261 (1983).
- [81] Y. Zhao, C. Lian, S. Zeng, Z. Dai, S. Meng, and J. Ni, Quartic anharmonicity and anomalous thermal conductivity in cubic antiperovskites A_3BO ($A = \text{K, Rb}; B = \text{Br, Au}$), *Phys. Rev. B* **101**, 184303 (2020).
- [82] X. Song, Y. Zhao, J. Ni, S. Meng, and Z. Dai, Strong anharmonic phonon scattering and superior thermoelectric properties of Li_2NaBi , *Mater. Today Phys.* **31**, 100990 (2023).
- [83] T. Yue, Y. Sun, Y. Zhao, S. Meng, and Z. Dai, Thermoelectric performance in the binary semiconductor compound $A_2\text{Se}_2$ ($A = \text{K, Rb}$) with host-guest structure, *Phys. Rev. B* **105**, 054305 (2022).
- [84] S. C. Rakesh Roshan, N. Yedukondalu, T. Pandey, L. Kunduru, R. Muthaiah, R. K. Rajaboina, L. Ehm, and J. B. Parise, Effect of atomic mass contrast on lattice thermal conductivity: A case study for alkali halides and alkaline-earth chalcogenides, *ACS Appl. Electron. Mater.* **5**, 5852 (2023).
- [85] G. Slack, Nonmetallic crystals with high thermal conductivity, *J. Phys. Chem. Solids* **34**, 321 (1973).
- [86] B. Peng, H. Zhang, H. Shao, Y. Xu, X. Zhang, and H. Zhu, Thermal conductivity of monolayer MoS_2 , MoSe_2 , and WS_2 : Interplay of mass effect, interatomic bonding and anharmonicity, *RSC Adv.* **6**, 5767 (2016).
- [87] C.-O. Romo-De-La-Cruz, Y. Chen, L. Liang, M. Williams, and X. Song, Thermoelectric oxide ceramics outperforming single crystals enabled by dopant segregations, *Chem. Mater.* **32**, 9730 (2020).
- [88] J. Mao, H. Zhu, Z. Ding, Z. Liu, G. A. Gamage, G. Chen, and Z. Ren, High thermoelectric cooling performance of n-type Mg_3Bi_2 -based materials, *Science* **365**, 495 (2019).
- [89] J. Mao, J. Zhou, H. Zhu, Z. Liu, H. Zhang, R. He, G. Chen, and Z. Ren, Thermoelectric properties of n-type ZrNiPb -based half-Heuslers, *Chem. Mater.* **29**, 867 (2017).
- [90] T. Sekimoto, K. Kurosaki, H. Muta, and S. Yamanaka, Thermoelectric and thermophysical properties of $\text{TiCoSb-ZrCoSb-HfCoSb}$ pseudo ternary system prepared by spark plasma sintering, *Mater. Trans.* **47**, 1445 (2006).
- [91] S. Li, H. Zhu, J. Mao, Z. Feng, X. Li, C. Chen, F. Cao, X. Liu, D. J. Singh, Z. Ren, and Q. Zhang, n-type TaCoSn -based half-Heuslers as promising thermoelectric materials, *ACS Appl. Mater. Interfaces* **11**, 41321 (2019).
- [92] W. Ren, X. Shi, Z. Wang, and Z. Ren, Crystallographic design for half-Heuslers with low lattice thermal conductivity, *Mater. Today Phys.* **25**, 100704 (2022).
- [93] Y. Xia and M. K. Y. Chan, Anharmonic stabilization and lattice heat transport in rocksalt β - GeTe , *Appl. Phys. Lett.* **113**, 193902 (2018).
- [94] W. Buhner and H. Bill, Lattice dynamics of Na_2S , *J. Phys. C* **13**, 5495 (1980).
- [95] W. Buhner and H. Bill, Phononen-dispersion in Na_2S , *Helv. Phys. Acta* **50**, 431 (1977).
- [96] T. Farley, W. Hayes, S. Hull, R. Ward, M. Hutchings, and M. Alba, The dynamic properties of lithium oxide investigated by neutron scattering techniques, *Solid State Ionics* **28-30**, 189 (1988).
- [97] L. Lindsay, D. A. Broido, and N. Mingo, Flexural phonons and thermal transport in graphene, *Phys. Rev. B* **82**, 115427 (2010).
- [98] T. Feng and X. Ruan, Four-phonon scattering reduces intrinsic thermal conductivity of graphene and the contributions from flexural phonons, *Phys. Rev. B* **97**, 045202 (2018).
- [99] B. S. Semwal and P. K. Sharma, Thermal conductivity of an anharmonic crystal, *Phys. Rev. B* **5**, 3909 (1972).
- [100] G. P. Srivastava and M. Prasad, Diagonal and nondiagonal Peierls contribution to the thermal conductivity of anharmonic crystals, *Phys. Rev. B* **23**, 4273 (1981).
- [101] X. Wang, Z. Gao, G. Zhu, J. Ren, L. Hu, J. Sun, X. Ding, Y. Xia, and B. Li, Role of high-order anharmonicity and off-diagonal terms in thermal conductivity: A case study of multiphase CsPbBr_3 , *Phys. Rev. B* **107**, 214308 (2023).
- [102] M. Simoncelli, N. Marzari, and F. Mauri, Unified theory of thermal transport in crystals and glasses, *Nat. Phys.* **15**, 809 (2019).
- [103] L. Isaeva, G. Barbalinardo, D. Donadio, and S. Baroni, Modeling heat transport in crystals and glasses from a unified lattice-dynamical approach, *Nat. Commun.* **10**, 3853 (2019).
- [104] A. Cepellotti and N. Marzari, Thermal transport in crystals as a kinetic theory of relaxons, *Phys. Rev. X* **6**, 041013 (2016).
- [105] J. Yue, J. Zheng, J. Li, S. Guo, W. Ren, H. Liu, Y. Liu, and T. Cui, Ultralow glassy thermal conductivity and controllable, promising thermoelectric properties in crystalline α - CsCu_5S_3 , *ACS Appl. Mater. Interfaces* **16**, 20597 (2024),.
- [106] J. Zheng, D. Shi, S. Liu, Y. Yang, C. Lin, Z. Chang, R. Guo, and B. Huang, Effects of high-order anharmonicity on anomalous lattice dynamics and thermal transport in fully filled skutterudite $\text{YbFe}_4\text{Sb}_{12}$, *Phys. Rev. Mater.* **6**, 093801 (2022).
- [107] Y. Xia, V. Ozoliņš, and C. Wolverton, Microscopic mechanisms of glasslike lattice thermal transport in cubic $\text{Cu}_{12}\text{Sb}_4\text{S}_{13}$ tetrahedrites, *Phys. Rev. Lett.* **125**, 085901 (2020).
- [108] T. Tadano and W. A. Saidi, First-principles phonon quasiparticle theory applied to a strongly anharmonic halide perovskite, *Phys. Rev. Lett.* **129**, 185901 (2022).
- [109] N. K. Ravichandran and D. Broido, Unified first-principles theory of thermal properties of insulators, *Phys. Rev. B* **98**, 085205 (2018).
- [110] M. Lazzeri, M. Calandra, and F. Mauri, Anharmonic phonon frequency shift in MgB_2 , *Phys. Rev. B* **68**, 220509(R) (2003).
- [111] T. Tadano, Y. Gohda, and S. Tsuneyuki, Impact of rattlers on thermal conductivity of a thermoelectric clathrate: A first-principles study, *Phys. Rev. Lett.* **114**, 095501 (2015).
- [112] J. Zheng, D. Shi, Y. Yang, C. Lin, H. Huang, R. Guo, and B. Huang, Anharmonicity-induced phonon hardening and phonon transport enhancement in crystalline perovskite BaZrO_3 , *Phys. Rev. B* **105**, 224303 (2022).